Polyoxometalates

RESEARCH ARTICLE

Hetero-motif PMo@VioPAFs for highly efficient photocatalytic degradation of antibiotics: Performance and synergistic mechanism

Shenzhen Chang [1,§], Jinhao Zhang[1,§], Yanhong Chen [2], Xiaofei Jing [3], Dongyu Guo [4], and Qinhe Pan [1]

[1] *Key Laboratory of Advanced Materials of Tropical Island Resources of Ministry of Education, School of Chemistry and Chemical Engineering, Hainan University, Haikou 570228, China*

[2] *Key Laboratory of Electrochemical Energy Storage and Energy Conversion of Hainan Province, School of Chemistry and Chemical Engineering, Hainan Normal University, Haikou 571158, China*

[3] *Key Laboratory of Polyoxometalate and Reticular Material Chemistry of Ministry of Education, Northeast Normal University, Changchun 130024, China*

[4] *Department of Clinical Laboratory, Xiamen Huli Guoyu Clinic, Co., Ltd, Xiamen 361000, China*

[§] *Shenzhen Chang and Jinhao Zhang contributed equally to this work.*

Received: 28 May 2026; **Revised:** 4 August 2026; **Accepted:** 27 August 2026

Address correspondence to Yanhong Chen, cyh3687@163.com; Dongyu Guo, xiamenhaijin@163.com; Qinhe Pan, panqh@hainanu.edu.cn

Cite This: *Polyoxometalates*, 2027, *6*, 9140157

Read Online

ABSTRACT: To mitigate the significant ecological and health threats posed by the pervasive discharge of emerging organic pollutants like antibiotics, developing robust, visible-light-responsive photocatalysts with high catalytic activity has emerged as a pivotal strategy for efficient wastewater remediation. Herein, a series of polyoxomolybdate-based viologen porous aromatic frameworks (PMo@VioPAFs) composites featuring hetero-motif structures were successfully synthesized via a mild self-assembly strategy. Driven by the strong electrostatic coupling between cationic VioPAF and anionic Keggin-type PMo clusters, the composite retains its structural integrity and delivers outstanding cycling stability. A key structural feature is the self-reduction property of viologen units, which induces the formation of low-valent molybdenum species, thereby multiplying available catalytic active sites. Furthermore, the hetero-motif heterostructure facilitates efficient separation and directional migration of photo-generated carriers. The optimized PMo@VioPAFs(2:1) exhibited superior photocatalytic performance, achieving >98% conversion of tetracycline within 50 min and total organic carbon removal efficiency reached nearly 80% within 90 min, significantly outperforming traditional POM-based systems. Mechanistic studies reveal a synergistic dual-site, dual-track reaction pathway, where direct hole-mediated oxidation and indirect radical-triggered ($\cdot O_2^-$ and $\cdot OH$) degradation coexist. This work provides a robust design template for high-efficiency, visible-light-active photocatalysts in recalcitrant wastewater treatment.

KEYWORDS: polyoxometalates; viologen porous aromatic frameworks; hetero-motif; photocatalytic; tetracycline.

1 Introduction

Alongside human society advances at a breakneck pace, the extensive exploitation of natural resources has enabled humanity to generate substantial wealth, yet it has also led to pervasive and severe contamination of the natural environment [1, 2]. Among these, antibiotics, as a critical class of pharmaceuticals, have been extensively utilized in modern society for the treatment of bacterial infections and the promotion of growth in animals and plants [3-5]. However, due to the poor absorption, slow metabolism, and high stability in organisms, coupled with inadequate management of their use and disposal, these pharmaceuticals have gradually emerged as pervasive contaminants in aquatic systems worldwide [4, 6-8]. Their persistence, ecotoxicity, and combined risks of inducing the spread of antibiotic resistance genes have raised significant concerns in the fields of environmental and public health, leading the World Health Organization to classify this issue as a major global public health challenge of the 21st century [7, 9, 10]. Therefore, developing efficient technologies to remove antibiotic contaminants from aquatic environments has become an urgent imperative. Although several methods, including physical adsorption, biodegradation, and conventional chemical oxidation, have been employed, certain limitations, such as low removal/degradation efficiency, incomplete mineralization, and potential secondary pollution, are frequently encountered with these approaches [11-13]. Against this backdrop, oxidation processes based on highly reactive oxygen species (ROS, *e.g.*, $\cdot OH$, $\cdot O_2^-$), particularly solar-driven photocatalysis, have shown great potential and emerged as a promising frontier due to their thorough mineralization under green and economical operating conditions [14-18]. Nevertheless, the design of efficient

photocatalysts remains a key challenge for the practical application of such technology.

Nanometer-sized, electron-rich polyoxometalates (POMs), constructed from high-valent early transition metals (e.g., W^{VI}, Mo^{VI}, V^{V}, etc.) have emerged as highly promising candidates in the realm of photocatalysis [19-24]. The electron-rich surface enables them to act as efficient electron donors, while the high-valence metal centers can function as electron sponges that participate in multi-electron transfer processes, thereby exhibiting remarkable photocatalytic activity [25-29]. Capitalizing on their rich structural diversity, reversible redox properties and excellent photoelectrochemical properties, POMs have been widely used in photocatalysis of redox reactions [30-32]. However, there are still plagued by several intrinsic drawbacks, including low specific surface area, high solubility in polar solvents, and a pronounced propensity for agglomeration and leaching. These issues not only lead to diminished catalytic activity but also complicate recyclability. More critically, pure POMs suffer from the rapid recombination of photogenerated electron-hole pairs and suboptimal quantum efficiency. Furthermore, an inherent trade-off exists within their band structure: achieving broad-spectrum photoresponse often comes at the expense of potent redox capability. This dual limitation constrains the utilization efficiency of visible light and attenuates the thermodynamic driving force of catalytic reactions.

Enhancing the separation efficiency of photogenerated carriers (electron-hole pairs) and suppressing their recombination is a critical determinant of photocatalytic performance [33-35]. Although the construction of semiconductor heterojunctions has become the well-established approach to broaden the light-responsive range and improve charge separation efficiency, traditional nanomaterials are often difficult to break through the performance bottleneck due to the size effects and limited interface contact areas [36-39]. More importantly, the traditional heterogeneous junctions lack accuracy at the atomic or molecular scale, resulting in the difficulty in regulating the distribution, spacing and interaction of redox sites, which seriously hinders the deep analysis of the structure-activity relationship [40]. Accordingly, in recent years, some forward-looking studies have focused on constructing hetero-motif systems by coupling POMs with porous organic frameworks (POFs) to enhance the stability and photocatalytic efficiency of POMs [41-44]. It is well known that POFs possess multifunctional porous structures, high conjugation, rich π-electrons, excellent stability, and good recyclability, which not only afford a platform for the homogeneous dispersion of POMs to effectively suppress agglomeration and leaching, but also enrich reaction substrates through the channel confinement effect to enhance mass transfer [42, 45-47]. More critically, intimate interfacial contact and effective electronic coupling can be established between POMs and the porous scaffolds, which facilitates the directional migration and spatial separation of photogenerated charge carriers, significantly curbing charge recombination. Meanwhile, the conjugated architecture and visible-light-harvesting capability of the framework materials broaden the spectral response range of the composite system, creating functional complementarity with the redox activity of POMs to yield a synergistic photocatalytic effect. For instance, Lan, Wang, An and other groups immobilized POMs within the channels of neutral covalent organic frameworks (COFs) *via* covalent or supramolecular interactions, successfully realizing heterogeneous catalysis for a suite of reactions including photocatalytic CO_2 reduction, water oxidation, and selective oxidation of sulfides [48-51]. Zhu and Tian et al. employed imidazolium-functionalized porous aromatic frameworks (iPAFs) as supports and observed a counterintuitive enhancement in the specific surface area of the composites upon incorporation of anionic POMs [52, 53]. These composites demonstrated remarkable catalytic activity and durability in oxidative desulfurization reactions.

Among the numerous POF structures available nowadays, two-dimensional viologen POFs (VioPOFs) based on the diquaternized 4,4′-bipyridine structural unit have attracted particular attention recently [54-56]. These materials not only preserve the highly reversible electron-transfer characteristics and favorable redox properties of the viologen units, but also overcome drawbacks of isolated viologen moieties such as broad energy level distribution and limited conjugation. Therefore, building hetero-motif POM-VioPOF systems is expected to provide a new ideas for developing a next-generation efficient photocatalytic systems; however, related research remains scarce [57-59]: (i) the hetero-motif structure facilitates rapid electron migration, thereby improving electron–hole separation efficiency; (ii) The porous framework of VioPOFs enables uniform dispersion of POMs at the molecular level; (iii) The positively charged skeleton of VioPOFs favors efficient adsorption of negatively charged polyanionic clusters; And (iv) the more accessible active sites will further enhance the catalytic performance of the system. Corroborating studies further underscore the efficacy of this strategy. An et al. engineered porphyrin-decorated, viologen-functionalized POFs to host POMs, achieving catalytic activity in the photoinduced selective oxidation of sulfides that rivals that of conventional thermal catalytic systems [58, 60]. In a parallel advancement, Hu and Chi et al. implemented a modular electrostatic assembly approach to immobilize monodisperse POM clusters onto VioPOFs. This hybrid architecture exhibited unique catalytic prowess in the electroreduction of furfural [57].

Based on the above advantages, a series of hetero-motif PMo@VioPAF photocatalytic systems with different loading ratios were successfully prepared by using phosphomolybdic acid (PMo) with strong oxidation and an absorption band edge of about 550 nm as an electron donor and two-dimensional viologen porous aromatic frameworks (VioPAFs) as an electron transfer medium (Scheme 1). Subsequent studies confirmed that VioPAFs not merely serve as a simple support but plays a critical role as an electron mediator. Specifically, effective electron transfer with PMo can be achieved, thereby facilitating the generation of reduced Mo^{5+} species with enhanced catalytic activity. Owing to this synergistic effect, such hetero-motif system exhibits far superior performance in the photocatalytic degradation of

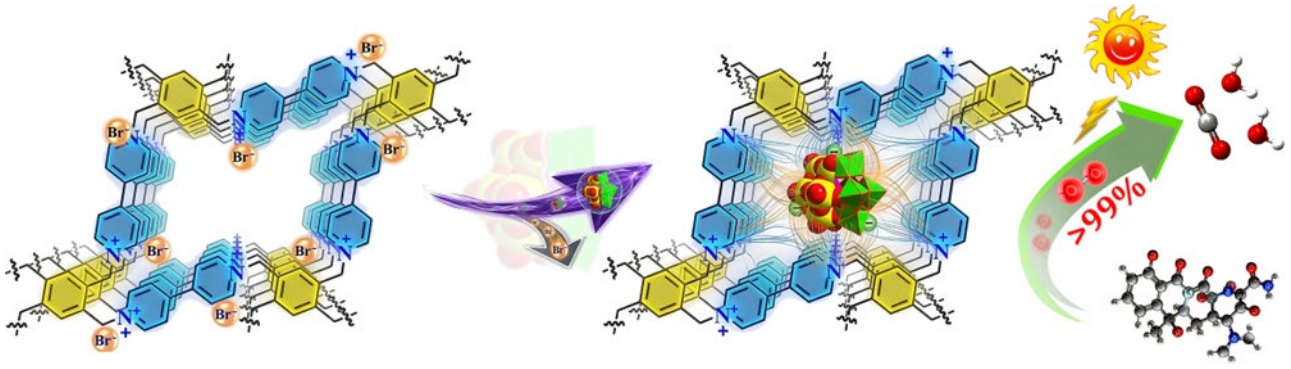

Scheme 1 Preparation process of PMo@VioPAFs and catalytic schematic diagram.

tetracycline (TC) compared with most reported POM-based heterojunction photocatalytic systems, achieving nearly 100% degradation within only 50 min. Furthermore, cyclic experiments have also confirmed that PMo@VioPAFs possesses excellent structural stability and durability.

2 Experimental

2.1 Materials

The detailed characterization techniques and synthesis of VioPAF are described in the Electronic Supplementary Material.

2.2 Synthesis of PMo@VioPAFs

PMo@VioPAFs was synthesized via a simple impregnation method. Specifically, 20 mg of PMo was weighed and placed in a beaker, followed by the addition of 10 mL of deionized water, and stirred until it was completely dissolved. After that, 10 mg of VioPAFs solid powder was added and stirred for 24 h under natural conditions at room temperature. After the reaction, the product was separated by suction filtration and washed with pure water for at least 5 times. The obtained solid was vacuum dried at room temperature for 9 h, and the blue-green solid powder was obtained after grinding treatment, which was recorded as PMo@VioPAFs(2:1), where 2:1 refers to the mass ratio of raw materials in the synthesis process.

By following the same synthetic procedure and only adjusting the mass ratio of PMo to VioPAFs, composites with different loading ratios could also be prepared, PMo@VioPAFs(1:3) and PMo@VioPAFs(1:1).

2.3 Typical process of photocatalytic oxidation degradation

A typical photocatalytic degradation experiment was conducted as follows: Firstly, 100 mL of TCs simulation solution with a concentration of 20 mg/L was accurately removed, and 10 mg of photocatalysts were added. The mixture was stirred continuously in the dark for 45 min to achieve adsorption-desorption equilibrium between the photocatalysts and TCs. Subsequently, the xenon lamp was switched on to initiate the photocatalytic reaction. Under visible light irradiation, a small aliquot of the reaction mixture was withdrawn at predetermined time intervals. This sample was filtered through a 0.45 μm membrane filter. The concentration of TC in the filtrate was then monitored at its characteristic wavelength of 357 nm using a UV-vis spectrophotometer to track the concentration changes.

The reaction condition exploration experiment follows the same procedure described above. Only a single variable in the system was changed, such as the type and amount of catalyst, the pH value of the reaction system (adjusted by dilute HCl and NaOH), etc.

3 Results and discussion

3.1 Synthesis

This study successfully prepared three photocatalysts by modulating the mass ratios of different synthetic precursors. The synthesis procedure is illustrated in Scheme 1. Initially, following a previously reported synthetic strategy, VioPAFs with a viologen skeleton was synthesized via the quaternization reaction between 4,4′-bipyridine and 1,2,4,5-tetrakisbromomethylbenzene [61]. The obtained product was systematically characterized by FT-IR and solid-state ^{13}C NMR spectroscopy (Fig. 1a and S1). The results confirmed the successful construction of VioPAFs. As can be seen from its structure, the VioPAF framework is rich in viologen units (4,4′-bipyridinium skeleton), and the corresponding counter anions are exchangeable Br^- ions, which can theoretically undergo strong electrostatic interactions with negatively charged polyoxoanions. Furthermore, it was found by determining the Zeta potential of VioPAFs under different pH conditions (Fig. S2) that the surface exhibits a significant positive charge in the strongly acidic environment formed by the PMo aqueous solution. This result further confirms that the framework carries a large number of positive charges under acidic conditions, which is conducive to the effective loading of anionic PMo species *via* electrostatic driving, thus achieving the controllable and efficient composite of PMo with the VioPAF matrix [62].

3.2 Characterization of the catalysts

To further confirm the structure of PMo@VioPAFs, a series of characterizations were performed. FT-IR spectroscopy analysis revealed that the characteristic peak of the VioPAFs at 1600 cm^{-1} remained intact after PMo loading, demonstrating the structural stability of its framework. Compared with pure VioPAFs, a new set of characteristic absorption peaks emerged for PMo@VioPAFs in the range of 1100-700 cm^{-1}. Taking PMo@VioPAFs(2:1) as an example (Fig. 1b), the peak at 1064 cm^{-1} was assigned to the stretching vibration of P—O_a bonds in the PMo framework. The two weak peaks at 742 cm^{-1} and 810 cm^{-1} corresponded to the stretching vibrations of Mo—$O_{b/c}$ bonds, while the intense

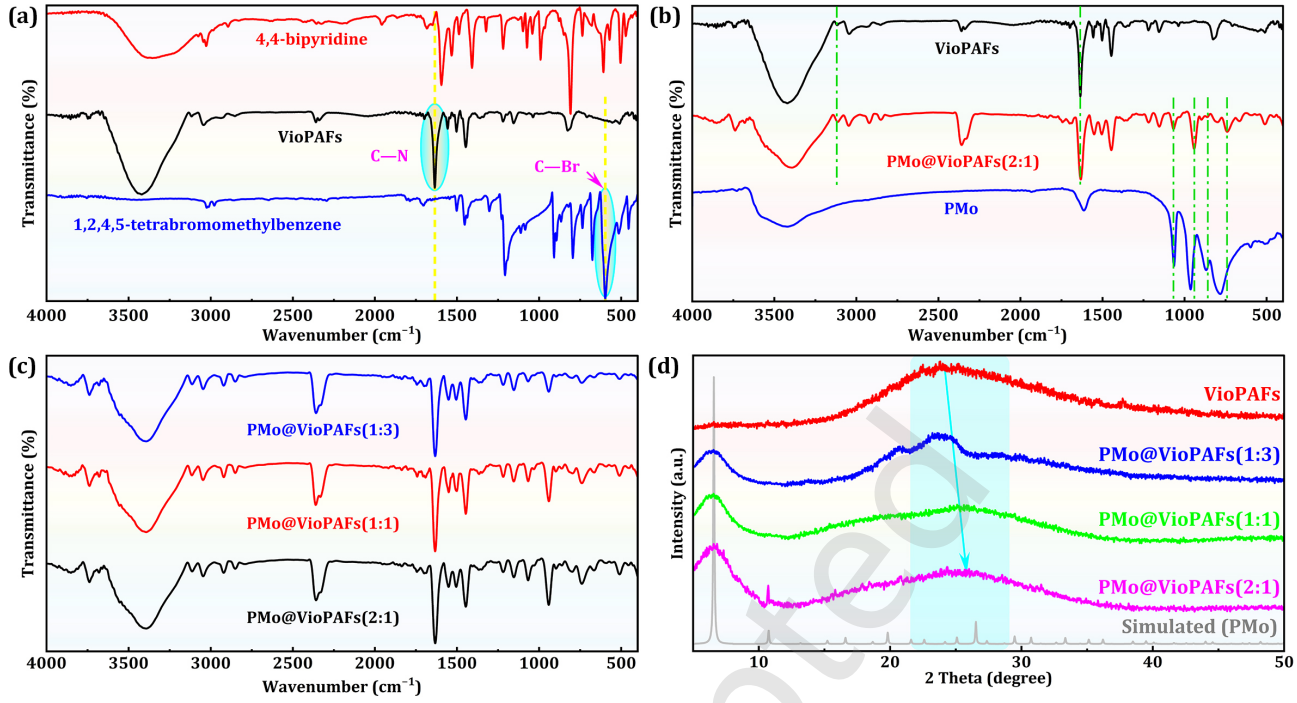

Figure 1 (a) The FT-IR spectra for VioPAFs and synthetic raw; (b) The FT-IR spectra for VioPAFs, PMo and PMo@VioPAFs(2:1); (c) The FT-IR spectra for PMo@VioPAFs with different loading ratios; (d) The PXRD patterns for different PMo@VioPAFs, VioPAFs, and simulated PXRD of PMo.

peak at 941 cm^{-1} was attributed to the vibration of $Mo=O_d$ bonds. Notably, these characteristic peaks of PMo exhibited a distinct shift relative to pure PMo, which confirmed the existence of strong interactions between PMo and the VioPAFs support. This phenomenon was also observed in PMo@VioPAFs(1:3) and PMo@VioPAFs(1:1) (Fig. S3 and S4). In addition, the absorption peaks of different catalysts showed obvious intensity differences, namely, the characteristic PMo peaks of PMo@VioPAFs(2:1) were significantly stronger than those of the other two catalysts (Fig. 1c), which could be ascribed to the variation in PMo loading amount.

A similar phenomenon was also prominent in the powder X-ray diffraction (PXRD) patterns (Fig. 1d). Specifically, the higher the PMo loading, the stronger the corresponding characteristic diffraction peak intensity, and the intensity ratio of these peaks to the main diffraction peaks of VioPAFs rose concomitantly, which directly reflects the gradual increase in PMo content within the composite. More crucially, the characteristic diffraction peaks of VioPAFs exhibited a systematic shift toward higher angles as the PMo loading amount increased. This peak shift indicates a reduction in the interplanar spacing, implying a slight yet ordered lattice contraction of the VioPAF framework after the introduction of PMo. This phenomenon not only further confirms the successful intercalation of PMo but also directly reveals the presence of strong electrostatic interactions between PMo anions and the positively charged viologen framework, and such interactions were continuously enhanced with the increasing PMo loading amount.

To approximately quantitatively determine the PMo loading amount in different composite systems and evaluate their thermal stability, thermogravimetric analysis (TGA) was employed to characterize the series of samples under a nitrogen atmosphere (Fig. 2a). Pure PMo exhibited a significant weight loss at about 100 °C, which can be attributed to the removal of crystal water. Pure VioPAFs also showed slight weight loss in the same temperature range, presumably due to the removal of physically adsorbed water. Notably, the VioPAF framework initiated a significant decomposition at around 300 °C, manifested as a pronounced mass loss, indicating that its thermal stability declined rapidly above this temperature. In comparison, the framework decomposition of PMo@VioPAF composites was distinctly delayed to the range of 350-400 °C, demonstrating that the strong electrostatic interactions between PMo anions and the positively charged viologen framework effectively enhanced the structural thermal stability of the VioPAFs. Furthermore, based on the differences in residual mass of each composite at the high-temperature stage (~800 °C) and in combination with the thermal weight loss behaviors of PMo and VioPAFs, the actual mass fractions of loaded PMo could be calculated, that is, the PMo content in PMo@VioPAFs(2:1) was approximately 44.38%, which was slightly higher than the 39.10% in PMo@VioPAFs(1:1) and significantly higher than the 30.64% in PMo@VioPAFs(1:3). The result was consistent with the trend of the initial feeding ratios, further confirming that the PMo loading amount in VioPAFs could be effectively regulated by adjusting the precursor ratio. Regarding the influence of the PMo-to-VioPAFs mass ratio on the photocatalytic performance, we did conduct exploration experiments with higher feed ratios (such as 3:1). The results showed that after further increasing the PMo feed ratio, the actual loading amount of the material did not continue to increase but remained basically the same as that of PMo@VioPAFs(2:1). We speculate that this might be due to the fact that the carrier has reached its maximum adsorption loading capacity under these conditions. Correspondingly, the subsequent photocatalytic degradation performance did not show significant changes.

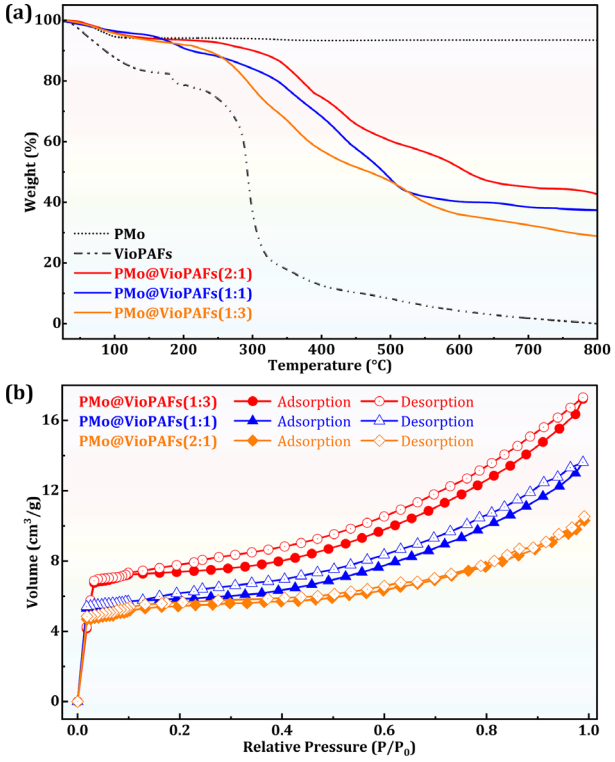

Figure 2 (a) The TGA curves for different PMo@VioPAFs, VioPAFs, and PMo; (b) Nitrogen adsorption-desorption isotherm curve for PMo@VioPAFs.

Similar results can be supported by the nitrogen adsorption-desorption isotherms (Fig. 2b and S5). It can be found that the specific surface area of the PMo@VioPAF composites decreases significantly compared to that of pure VioPAFs, directly proving the successful loading of PMo. Moreover, the adsorption-desorption isotherms of all three PMo@VioPAF composites exhibit typical type-IV characteristics with distinct hysteresis loops, indicating that the mesoporous structure of the VioPAFs remains intact after PMo loading. Concurrently, the specific surface area of PMo@VioPAFs(2:1) is lower than those of PMo@VioPAFs(1:1) and PMo@VioPAFss(1:3), indicating that with the increase of PMo dosage, the actual load in the composite material gradually increased, which is consistent with the above conclusion. When the number of POMs was further increased, the specific surface area does not continue to decrease, implying that PMo@VioPAFs(2:1) may be close to the maximum loading capacity within this system.

The surface electronic structure of the prepared samples was systematically characterized by X-ray photoelectron spectroscopy (XPS), aiming to reveal the influence of PMo on the electronic environment of VioPAFs before and after loading. Fig. 3 shows the full-spectrum scan of VioPAFs and PMo@VioPAFs(2:1) samples and the high-resolution XPS spectra of Mo 3d and N 1s orbitals. As shown in Fig.3a, compared with the original VioPAF sample, the full spectrum of PMo@VioPAFs(2:1) showed an obvious Mo 3d characteristic peak at the binding energy of about 233 eV, which clearly confirmed the successful loading of PMo. Further analysis of the N 1s high-resolution spectrum (Fig.3b) shows that the N 1s signal in VioPAFs exhibits two characteristic peaks. The peak at 400.4 eV is attributed to the

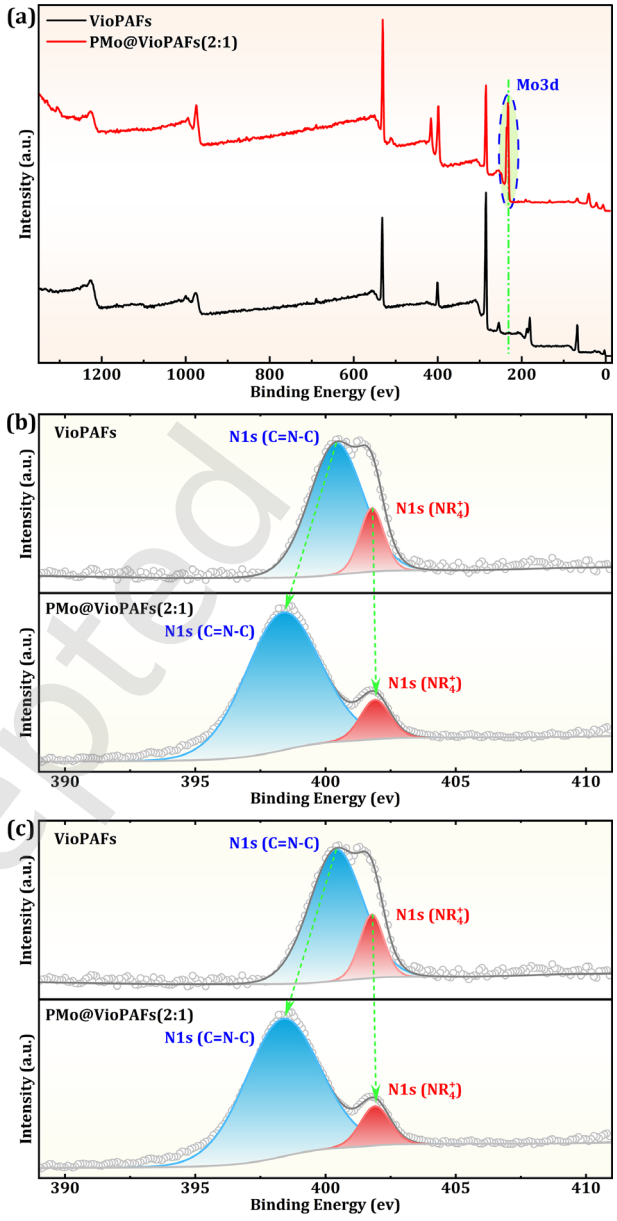

Figure 3 (a) XPS full spectra, (b) high-resolution scan of N1s electron, and (c) high-resolution scan of Mo3d electron for PMo@VioPAFs(2:1).

nitrogen atom in the imine bond (C=N—C), and the peak at 401.8 eV corresponds to the quaternary ammonium nitrogen species (NR_4^+). It is worth noting that in PMo@VioPAFs(2:1), the binding energies of these two nitrogen species are significantly shifted to 398.4 eV and 401.9 eV, respectively, indicating that the introduction of PMo interacts with the nitrogen sites in the VioPAF skeleton, which may be due to electrostatic attraction, thus changing the local electron density. Similarly, an obvious chemical shift phenomenon was also observed in the Mo 3d high-resolution spectrum (Fig.3c). Specifically, the typical Mo^{6+} characteristic double peaks (Mo $3d_{5/2}$ and Mo $3d_{3/2}$) in PMo before loading are located at 235.8 eV and 236.5 eV, respectively, while in PMo@VioPAFs(2:1), the two peaks move to 232.6 eV and 233.4 eV in the direction of low binding energy, which are still attributed to the Mo^{6+} species, and the displacement further confirms the electronic coupling between the Mo center and the VioPAF skeleton. More importantly, a new pair of characteristic peaks at 231.4 eV and 234.5 eV can be attributed to the $3d_{5/2}$ and $3d_{3/2}$

orbitals of Mo, indicating that part of Mo^{6+} is reduced to Mo^{5+} during the recombination process. This reduction phenomenon is also visually corroborated by the color change of the sample from the brownish-yellow of pristine VioPAFs to the green of PMo@VioPAFs(2:1) (Fig. S6). We speculate that this reduction process may stem from the weak reducing effect of electron-rich groups in the VioPAF framework (such as imine nitrogen or aromatic rings) on Mo^{6+} under the open aqueous-phase synthesis conditions, which promotes the conversion of a small amount of Mo^{6+} to Mo^{5+}. Based on quantitative fitting of the peak areas of Mo^{5+} and Mo^{6+} in the XPS spectrum, the molar ratio of Mo^{5+}/Mo^{6+} is calculated to be approximately 0.20, corresponding to a total mass fraction of Mo^{5+} in the sample of about 4.2 wt%. The partial reduction of POMs during immobilization has been extensively reported in the literature. Moreover, our prior studies have demonstrated that the presence of Mo^{5+} species can effectively modulate the electronic structure of the material, enhance its charge-transfer capability, and thereby significantly boost its activity in catalytic reactions [62].

3.3 Photoelectric performance analysis of catalysts

As a proof of concept, we first evaluated the performance of PMo@VioPAFs in enhancing visible light absorption through ultraviolet-visible diffuse reflectance spectroscopy (UV-vis DRS). As shown in Fig. 4a, compared to pure PMo and VioPAFs, PMo@VioPAFs exhibits multiple absorption peaks in the UV-vis region, which can be broadly categorized into two types: (i) notable absorption peaks in the short- to mid-wave UV region (200-400 nm), primarily attributed to $\pi \rightarrow \pi^*$ transitions in the viologen ligand; (ii) absorption peaks in the range of 400-500 nm, likely originating from $O \rightarrow Mo$ charge transfer in the polyoxoanions, with a slight red shift compared to pure PMo, possibly due to the presence of reduced Mo^{5+} species. Based on Kubelka-Munk analysis, the band gap of PMo@VioPAFs(2:1) is 2.26 eV, lower than that of pure PMo (2.39 eV) and pure VioPAFs (2.78 eV) (Fig. 4b). Furthermore, its band gap is further reduced compared to PMo@VioPAFs(1:1) (2.30 eV) and PMo@VioPAFs(1:3) (2.39 eV) with lower PMo loadings (Fig. S7-S8), indicating that increasing the PMo loading can effectively modulate the band gap of the composite material. This modulation favors the separation and migration of photogenerated electrons, thereby demonstrating theoretical potential as an efficient catalyst [58].

Through Mott-Schottky tests at different frequencies (Fig. 4c, Fig. S9-S10), it was found that all three PMo@VioPAFs with different loading ratios exhibited typical n-type semiconductor characteristics (with positive slopes in the curves). For PMo@VioPAFs(2:1), the flat band potential determined from its intercept was approximately −0.82 V (*vs.* Ag/AgCl), corresponding to the conduction band (CB) energy level of about −0.62 V (*vs.* NHE). This value is lower than the reduction potential of $O_2/\cdot O_2^-$ (−0.33 V *vs.* NHE). By combining Kubelka-Munk analysis with Mott-Schottky plots, the valence band (VB) energy level of PMo@VioPAFs(2:1) was calculated to be +1.64 V (*vs.* NHE). Similarly, the CB energy levels of PMo@VioPAFs(1:1) and PMo@VioPAFs(1:3) are −0.78 V and −0.68 V, respectively, while the VB energy levels are +1.52 V and +1.71 V, respectively. The CB level of PMo@VioPAFs(2:1) is lower than those of the other two composites, suggesting that it may possess higher photocatalytic activity. Compared with the corresponding values for pure VioPAFs and pure PMo (Fig. 4d, Fig. S11-S12), the CB levels of all composites are closer to the activation potential of molecular oxygen, and thus they are all theoretically suitable as efficient catalysts under visible light for pollutant degradation [62, 63].

Furthermore, the photogenerated charge separation and transfer efficiency of the prepared photocatalysts was evaluated by transient photocurrent measurements. As

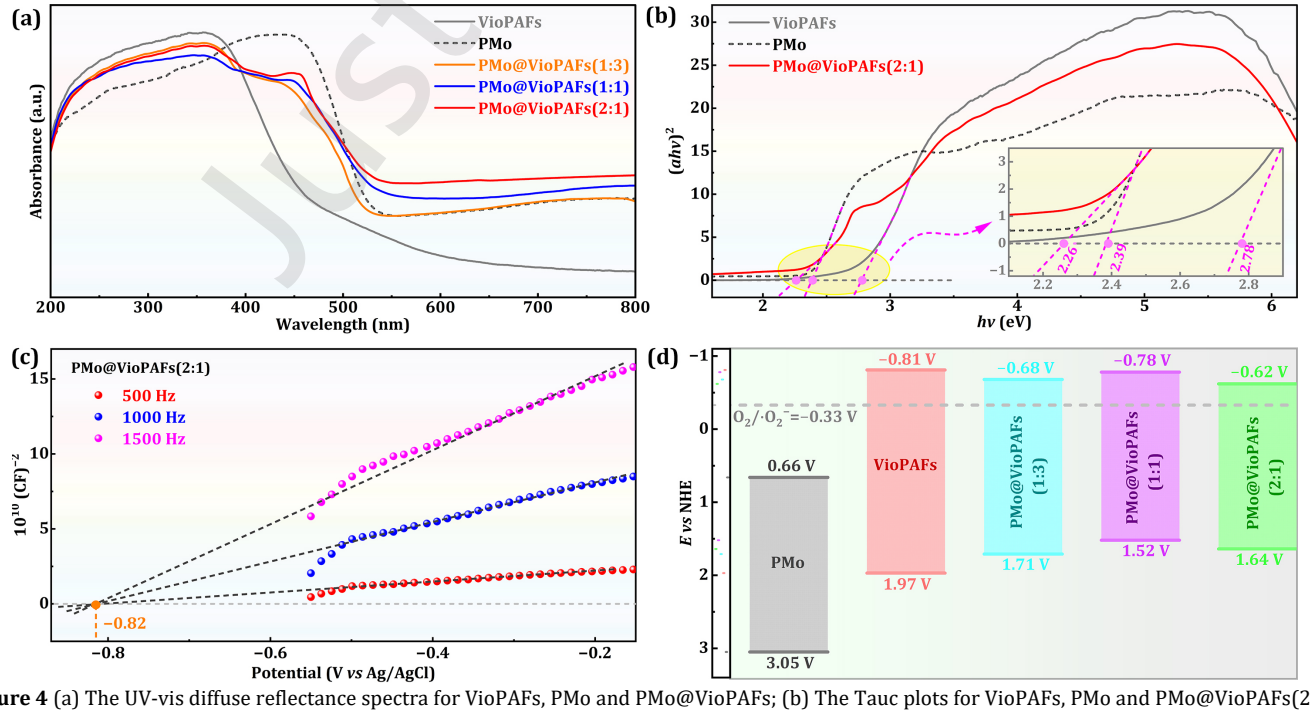

Figure 4 (a) The UV-vis diffuse reflectance spectra for VioPAFs, PMo and PMo@VioPAFs; (b) The Tauc plots for VioPAFs, PMo and PMo@VioPAFs(2:1); (c) The Mott-Schottky plots for PMo@VioPAFs(2:1); (d) The Energy band structures for different VioPAFs, PMo and PMo@VioPAFs.

shown in Fig. 5, a series of hetero-motif materials all exhibited stable and reversible photocurrent responses under visible light irradiation; however, no significant photocurrent signal was detected for pure PMo. Notably, the loading amount of PMo plays a significant modulating role in the photocurrent response of the composites, with the photocurrent intensity following the order PMo@VioPAFs(2:1) > PMo@VioPAFs(1:1) > PMo@VioPAFs(1:3) > VioPAF. This indicates that PMo@VioPAFs(2:1) possesses the highest photogenerated electron-hole pair separation efficiency, which can effectively suppress the recombination of photogenerated charge carriers.

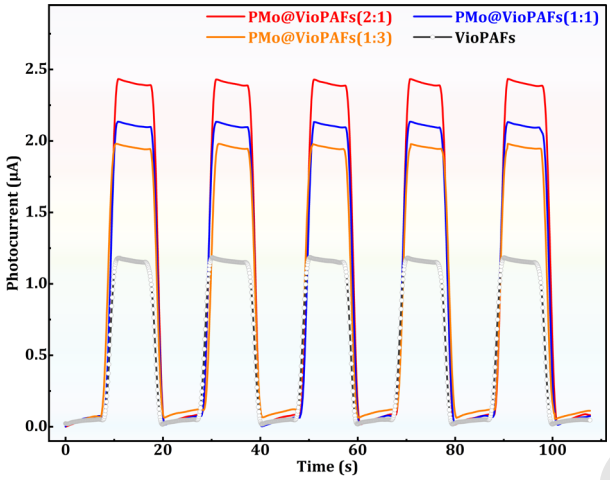

Figure 5 Transient photocurrent responses for PMo@VioPAFs and VioPAFs.

3.4 Photocatalytic degradation of tetracycline

Currently, POM-based heterogeneous photocatalytic systems have been reported for the photocatalytic degradation of antibiotics, yet their catalytic conversion efficiency still has considerable room for improvement. This study provides the first evidence that the PMo@VioPAFs composite exhibits excellent performance and application potential in the photocatalytic oxidative degradation of TCs under visible light irradiation in an oxygen atmosphere (Fig. 6). Experimental results show that the PMo@VioPAFs(2:1) displays the optimal photocatalytic activity. Under ambient conditions, after 50 min of visible light exposure, its conversion efficiency for TCs reaches 98.1% and the total organic carbon (TOC) removal efficiency was 69.6% (Fig. 6a and Table S1). Under the same reaction conditions, pure PMo and pure VioPAFs exhibit degradation efficiencies of only 17.4% and 44.7%, respectively, significantly lower than the composite catalytic material. Furthermore, for comparison, the catalytic results of the mixture prepared by the physical mixing method of PMo + VioPAFs showed that such system could achieve a conversion rate of 55.3% (Table S1). These results indicate that the superior catalytic performance of the composite catalyst stems from the synergistic effect between PMo and VioPAFs, rather than a simple additive effect of individual components. As the reaction time increases, the degradation efficiency of PMo@VioPAFs(2:1) for TCs can be further enhanced, but the rate of improvement slows markedly. When the reaction time is extended to 90 min, the conversion efficiency increases only to 99.2%, meaning that a 40-minute extension leads to a mere 1.1 percentage point gain. Notably, the TOC removal rate increased by approximately 10 percentage points, reaching 79.4% (Table S1). Some of the undegraded products may belong to the small molecule intermediates generated by the ring-opening reaction (Table S2). Furthermore, after 50 min of visible light irradiation, PMo@VioPAFs(1:1) and PMo@VioPAFs(1:3) achieve degradation efficiencies of 82.0% and 69.5%, respectively (Fig. 6a). This trend aligns with the earlier photo-electrochemical analysis, indicating that tuning the loading amount of PMo effectively optimizes the photocatalytic performance of the composite. When the reaction time is prolonged to 90 min, the degradation efficiencies of PMo@VioPAFs(1:1) and PMo@VioPAFs(1:3) increase to 87.4% and 81.4%, representing gains of 5.4% and 11.9% compared to the 50-minute results. This is mainly because the two samples had not yet reached degradation equilibrium at 50 min, leaving substantial room for further reaction.

In the dark adsorption equilibrium stage of 45 min, pure VioPAFs without PMo loading achieved a TCs adsorption capacity of 32.0%. As the PMo loading increased, the adsorption capacity of the composites for TCs showed a significant declining trend, with the highest-loaded PMo@VioPAFs(2:1) reaching only 15.4% adsorption (Fig. 6a). The results show that the loading of PMo will occupy the adsorption active site of the substrate on VioPAFs, resulting in a decrease in the adsorption capacity and mass transfer efficiency of the material. However, this adverse effect is much smaller than the active gain brought about by electronic regulation. The net outcome of this trade-off manifests as an overall enhancement in photocatalytic efficiency. On one hand, although the mass transfer rate experiences a marginal decline, it does not constitute the rate-determining step. Despite a reduction in BET specific surface area, the host framework of VioPAFs remains unobstructed, preserving intact mesoporous channels within the composite. Concurrently, the incorporation of PMo introduces additional chemisorption sites *via* electrostatic interactions and surface complexation, effectively compensating for the negative impact caused by the loss of physical surface area. On the other hand, the activity gain stemming from electronic structure modulation assumes a decidedly dominant role. As prototypical electron acceptors, PMo units construct a hetero-motif architecture with VioPAFs capable of efficiently trapping photogenerated electrons. This drastically suppresses carrier recombination. This substantial elevation in intrinsic reactivity far surpasses the minor penalty incurred by slightly diminished mass transport, serving as the core driver behind the marked performance improvement of the composite photocatalyst. Nevertheless, should the PMo loading prove excessive, mass transfer resistance would elevate from a secondary factor to the dominant limiting factor. Severe pore blockage induced by overloading drastically diminishes mass transport efficiency within the reaction system, thereby exerting a pronounced detrimental effect on catalytic performance. Integrating the experimental results of catalytic activity and adsorption behavior, PMo@VioPAFs(2:1) is identified as the optimal PMo loading ratio in this series of materials.

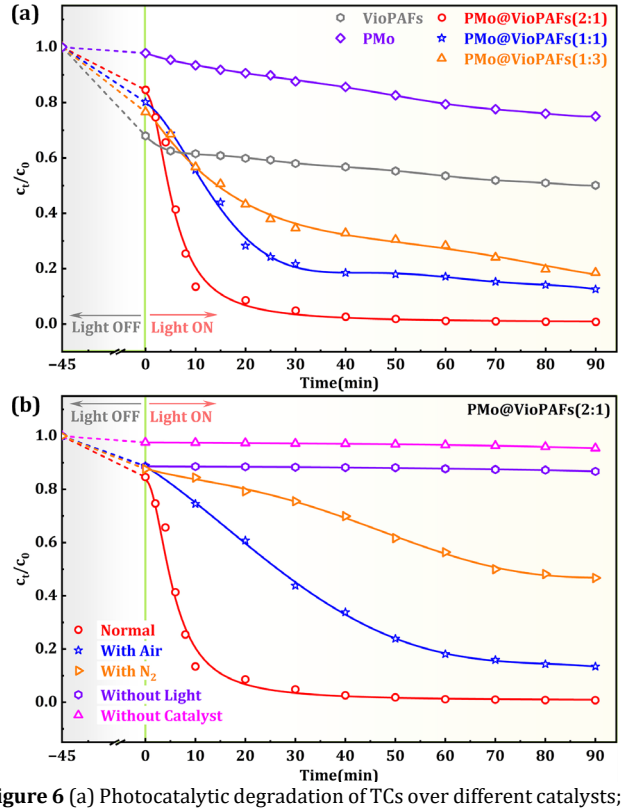

Figure 6 (a) Photocatalytic degradation of TCs over different catalysts; (b) Photocatalytic performance of PMo@VioPAFs(2:1) under different conditions.

When the oxidant in the reaction system was changed from pure oxygen to air, the photocatalytic performance of the material exhibited a slight decrease, with a TCs degradation efficiency of 86.5% at 90 min (Fig. 6b). This indicates that oxidant concentration is a key factor in regulating the reaction efficiency of the catalytic system. Notably, even when the oxidant was removed and the system was placed under a nitrogen inert atmosphere, degradation of TCs could still occur, reaching 53.3% at 90 min. Based on the dark adsorption experiment results, the contribution of physical adsorption could be ruled out, confirming that this process corresponds to the chemical conversion of tetracycline. Combined with subsequent mechanistic analysis, it can be inferred that the degradation activity under the inert atmosphere originates from the direct oxidation by the empty orbitals of photoexcited POMs. Blank control experiments demonstrate that both light and the catalyst are essential for this photocatalytic system. In the absence of either catalyst or light, the removal rates of tetracycline at 90 min were only 4.5% and 13.3%, respectively (Fig. 6b), values comparable to the adsorption capacity observed during the dark adsorption equilibrium stage. This indicates that under these conditions, the reduction in TCs concentration stems solely from physical adsorption, with no significant photocatalytic degradation occurring. In summary, the excellent photocatalytic degradation performance of this catalytic system is jointly determined by the synergistic interplay of light, catalyst, and oxidant concentration.

In-depth analysis of the photocatalytic degradation data for PMo@VioPAFs(2:1) reveals that its apparent kinetics for TCs degradation lie between first-order and second-order models (Fig. S13-S14). Notably, this deviates from the *pseudo*-first-order kinetics typically observed in conventional low-concentration photocatalytic systems governed by the Langmuir-Hinshelwood (L-H) model. We hypothesize that this kinetic divergence stems primarily from the following mechanisms [64]. First, photoactive species-dominated *quasi*-steady-state behavior. Photocatalysis involves highly unstable intermediates such as free radicals. As photoactivated products, the concentrations of these reactive species and their catalytic rate constants fluctuate dynamically with factors like light intensity and reaction time. Consequently, the system aligns more closely with the *quasi*-steady-state assumption rather than the thermodynamic equilibrium of adsorption-desorption presupposed in the classical L-H model. Furthermore, the catalyst's abundant active sites facilitate strong chemisorption of target pollutants via surface complexation and electrostatic interactions. This sustains an exceptionally high local adsorbate density on the catalyst surface even at low bulk pollutant concentrations, decoupling the reaction rate from the concentration of adsorbed substrates.

3.5 Optimization of photocatalytic reaction conditions

In the process of exploring catalytic performance, we systematically optimized the photodegradation conditions for TCs using a PMo@VioPAFs(2:1) catalytic system. Catalyst dosage is a core variable influencing photocatalytic performance and cannot be overlooked (Fig. 7a). For this system, initial investigations were conducted with a dosage of 5 mg. The results showed that under this condition, PMo@VioPAFs(2:1) achieved a TCs degradation rate of 81.3% within 90 min. As the catalyst dosage increased, the photocatalytic activity of the system improved significantly. When the dosage was raised to 10 mg, a 98.1% TCs conversion rate was achieved within just 50 min. However, excessive catalyst addition led to over-dispersion of solid-phase powder in the heterogeneous system, causing shading and scattering effects on incident light. This hindered photon capture by the catalyst, thereby diminishing light utilization efficiency. For instance, with a catalyst dosage of 20 mg, the TCs conversion rate after 90 min of reaction was only 96.1%. These findings indicate that increasing the catalyst dosage within an appropriate range effectively enhances the photocatalytic degradation performance of the system.

Oxidant type and concentration are another core factor influencing photocatalytic reaction efficiency. The above results have confirmed that the oxidative degradation effect of the system is significantly better than that of the air system when pure oxygen is used as the oxidant (Fig. 6b). It is well known that the volume fraction of oxygen in air is only 21%, much lower than the oxygen concentration in a pure oxygen system. Higher oxygen concentrations facilitate fuller contact with the catalyst surface, thereby allowing oxygen to be activated by photogenerated electrons to generate superoxide radicals, which accelerates the oxidation process. Notably, even when the oxygen concentration in the system is reduced to nearly zero, the conversion rate of TCs does not drop to zero but remains around 53.3%. This indicates the existence of a non-radical reaction pathway in this catalytic system that does not depend on oxygen activation.

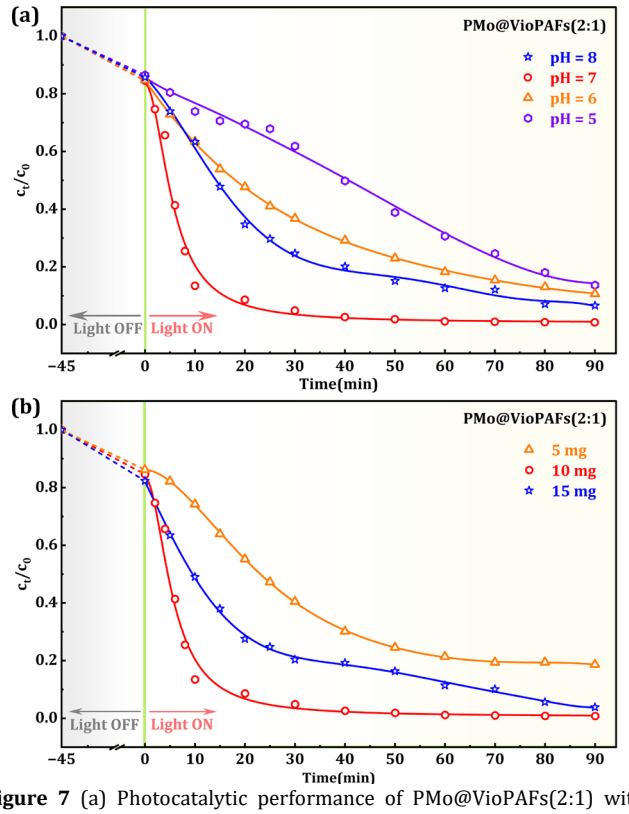

Figure 7 (a) Photocatalytic performance of PMo@VioPAFs(2:1) with different dosages; (b) Photocatalytic performance of PMo@VioPAFs(2:1) at different pH values.

To investigate the influence of pH on the degradation performance of TCs, a series of photocatalytic experiments were conducted within the pH range of 5 to 8 (Fig. 7b). The results indicate that the degradation efficiency of TCs generally increased with rising pH, reaching its peak at pH 7. This phenomenon is primarily attributed to the regulation of the adsorption-degradation process by electrostatic interactions between TCs and the photocatalyst surface. TCs exists in different dissociation species in aqueous solutions depending on pH. When pH < 3.3, TC mainly exists as the positively charged TCH_3^+. If the pH is between 3.3 and 7.7, TCs is mainly in the form of neutral TCH_2. And TCs are dissociated into negatively charged TCH^- or TC^{2-} only when the pH exceeds 7.7 [63]. Zeta potential measurements clarified the surface charge characteristics of PMo@VioPAFs(2:1) under different pH conditions. Its surface positive charge density gradually decreased as pH increased (Fig. S2). Based on these findings, it can be inferred that under acidic conditions, the catalyst surface becomes protonated and positively charged, leading to electrostatic repulsion with the cationic form of TCs, thereby reducing TCs adsorption capacity. Under weakly alkaline conditions, both the catalyst and TC carry negative charges, and the electrostatic repulsion between them similarly inhibits the adsorption process. This is one of the key reasons why TCs degradation efficiency at pH = 8 was lower than that at pH = 7. Additionally, under alkaline conditions, the loaded PMo may partially detach, resulting in a reduction of active sites and a further decrease in photocatalytic degradation efficiency. In contrast, at pH = 7 (neutral conditions), the surface charge properties of PMo@VioPAFs(2:1) best match the neutral dissociation form of TCs, enabling efficient TC adsorption. Therefore, in all subsequent experiments, the solution pH was adjusted to 7.

Although reaction temperature is an important parameter affecting catalytic efficiency, considering that room-temperature operation offers better economic feasibility and engineering applicability in practical water treatment scenarios, all photocatalytic experiments in this study were conducted at room temperature without additional temperature control.

3.6 Compared with other POM-based photocatalytic systems for oxidative degradation of TCs

To date, reports on POM-based heterogeneous photocatalytic systems for the oxidative degradation of TCs remain limited. Most reported systems are constructed using a POM-loading strategy, with metal oxide semiconductors being the most commonly used photoactive supports. Shi et al. prepared a $Bi/PMo_{12}/TiO_2$ composite photocatalyst comprising mesoporous PMo_{12}-doped TiO_2 loaded with Bi nanoparticles. The optimal sample with 20% loading achieved a TCs degradation efficiency of only 86.0% within 60 min under visible light irradiation (Table 1, Entry 2) [65]. Wang et al. constructed $SnO_2/PW_{12}/TiO_2$ core-interlayer-shell coaxial nanofibers via electrospinning, in which phosphotungstic acid (PW_{12}) served as a crucial interfacial layer, forming tandem heterojunctions of TiO_2/PW_{12} and PW_{12}/SnO_2. This material showed a TCs degradation efficiency of merely 73.8% within 30 min under visible light (Table 1, Entry 3) [66], and the study did not conduct an in-depth investigation into the structure-activity relationship or application potential of the system. Hu et al. synthesized an artificial-chloroplast-structured HPW_x/Fe_2O_3-CNTs photocatalyst via successive hydrothermal and microwave irradiation methods. This material achieved 100% TCs degradation within 100 min under mild conditions, with an apparent reaction rate constant 5.5 times that of pure Fe_2O_3 (Table 1, Entry 4) [67]. Li et al. fabricated CuPOMs/ZnO/PDA nanocomposites, which exhibited a photocatalytic degradation efficiency of 90.75% for TCs within 90 minutes. Even in the presence of competing co-existing substances in water, it maintained a TC removal rate of nearly 80% (Table 1, Entry 5) [68]. Liang et al. synthesized a heterojunction catalyst comprising Fe-POM-modified Bi_2MoO_6 with exposed {010} highly active crystal facets. This material demonstrated excellent photo-Fenton degradation performance over a wide pH range, achieving complete TCs degradation (100%) within 18 min. It is important to note, however, that this system required H_2O_2 as an additional oxidant (Table 1, Entry 6) [69].

Xing et al. constructed a hollow core-shell structured $PMo_{12}/CdS/Bi_2S_3$ Z-scheme tandem heterojunction. This material showed a TCs photocatalytic degradation efficiency of only 97.51%within 120 min under visible light (Table 1, Entry 7) [70]. Shi et al. developed an S-scheme core-shell heterojunction, $CsPMo_{12}/MnIn_2S_4$, whose optimally proportioned sample achieved a tetracycline removal rate of 97.81% within 60 min under visible light (Table 1, Entry 8) [71]. Tan et al. prepared a 1D/2D Z-scheme $AgPMo_{12}/g\text{-}C_3N_4$ photocatalyst via a self-assembly strategy. Although this composite exhibited some TCs degradation activity under visible light, the degradation rate was only about 50% within

Table 1 Comparison of POM-based photocatalytic systems for oxidative degradation of TCs

Entry	Cat.[a]	Amt. (mg)	Light	Conc. (mg/L)	Conv. (%)	Time (min)	MNR (× 10^{-3} h^{-1})[b]	Ref.
1	**PMo@VioPAFs(2:1)**	**10**	**300 W Xe lamp**	**20**	**98.1**	**50**	**235.4**	**This work**
2	$Bi/PMo_{12}/TiO_2$	20	300 W Xe lamp	20	86	60	17.2	[65]
3	$SnO_2/PW_{12}/TiO_2$	10	300 W Xe lamp	20	73.8	30	295.2	[66]
4	PW_x/Fe_2O_3-CNTs	20	300 W Xe lamp	10	99.99	100	24	[67]
5	Cu-POMs/ZnO/PDA	50	300 W Xe lamp	50	90.75	90	60.5	[68]
6	$FePW_{12}/Bi_2MoO_6$[c]	20	5 W LED	20	100	18	166.67	[69]
7	$PMo_{12}/CdS/Bi_2S_3$	30	300 W Xe lamp	10	97.51	120	4.88	[70]
8	$CsPMo_{12}/MnIn_2S_4$	20	300 W Xe lamp	20	97.81	60	19.56	[71]
9	$AgPMo_{12}/g\text{-}C_3N_4$	20	300 W Xe lamp	20	52	40	15.6	[72]
10	$NR\text{-}AgPMo_{12}$	50	500 W Xe lamp	20	40	180	2.67	[73]
11	$NR\text{-}AgPMo_{12}$/CuPc	50	500 W Xe lamp	20	61	180	4.07	[73]
12	$NP\text{-}AgPMo_{12}$	50	500 W Xe lamp	20	29	180	1.93	[73]
13	PW_{12}@ZIF-8/AuNP	0.6[d]	125 W Hg lamp	10	86	60	14.33	[74]
14	$CuPW_{12}/AgCl/Ag$	100	500 W Xe lamp	20	85	120	8.5	[75]
15	$Ag/Ag_3PO_4/AgPMo_{12}$	10	500 W Xe lamp	30	97	180	97	[76]
16	$FeMo_4$-TPT	10	300 W Xe Lamp	10	98.1	60	4.91	[17]
17	$TbMo_8\text{-}L_1$	10	300 W Xe lamp	15	92.71	120	13.91	[77]

[a]Summary based on key features of the cited literature;
[b]"MNR" stands for mass-normalized rate or apparent degradation rate, calculated according to the formula: (TC Concentration × Volume × Conversion) / (Catalyst Amount × Time) × 1000;
[c]Oxidant is H_2O_2 (all others use O_2);
[d]Unit is g/L.

40 min (Table 1, Entry 9) [72]. Li et al. prepared a series of pure-phase POM nanorods and combined them with phthalocyanine to construct Type II heterojunction photocatalysts. However, the resulting composites showed poor catalytic performance for TCs degradation, with the highest conversion rate after 180 min being only approximately 60% (Table 1, Entries 10-12) [73].

The Shahrak's group prepared a composite structure of gold nanoparticle-decorated polyoxometalate/zeolitic imidazolate framework-8 (PW_{12}@ZIF-8/AuNP). This material had a bandgap of only 1.13 eV, much lower than that of pure ZIF-8, and could remove tetracycline from water via an adsorption-photocatalysis synergy. At pH = 7, the degradation rate for TCs was 86% within 60 min (Table 1, Entry 13) [74]. The Li's group synthesized a Z-scheme $CuPW_{12}/AgCl/Ag$ photocatalyst via a hydrothermal-chemical co-precipitation method. Under simulated sunlight irradiation, the TCs degradation rate reached 86% within 120 min (Table 1, Entry 14) [75]. The S-scheme heterojunction $Ag/Ag_3PO_4/AgPMo_{12}$ developed by Wang et al. achieved a TCs degradation efficiency of 97% within 180 min under visible light (Table 1, Entry 15) [76].

It is noteworthy that some crystalline porous materials have also demonstrated certain photocatalytic activity for TCs degradation. For example, Han et al. prepared a Fe-based MOF photocatalyst containing Mo(VI) clusters, $FeMo_4$-TPT, which achieved a photocatalytic degradation rate of 98.01% for TCs within 60 min under mild conditions using oxygen as the oxidant (Table 1, Entry 16) [17]. Similarly, Niu et al. synthesized a series of polyoxometalate-based metal-organic complex photocatalysts, with the optimal sample achieving a TCs degradation rate of about 93% within 120 min (Table 1, Entry 17) [77].

In this work, we report, for the first time, the application of POM-based VioPAFs material for the efficient photocatalytic degradation of TCs. Performance comparison reveals that the PMo@VioPAFs(2:1) system developed in this study exhibits significantly superior catalytic performance compared to the vast majority of reported polyoxometalate-based photocatalytic systems. It achieves near-complete TCs conversion in just 50 min (Table 1, Entry 1). Notably, among photocatalytic systems using oxygen as the sole oxidant, the activity of this material, while achieving near-total TCs degradation, ranks among the highest levels reported for similar systems to date (Fig. 8a). This study not only provides a novel high-performance catalytic system for the efficient removal of TCs from water but also offers new research insights and experimental references for the subsequent structural design, interface modulation, and performance optimization of POM-based photocatalysts.

3.7 Photocatalytic cycling stability

The reusability and structural stability of catalysts are core indicators for evaluating the practical application value of heterogeneous catalysts. As shown in Fig. 8b and S15, after each catalytic reaction, an equal amount of substrate was replenished into the system. The PMo@VioPAFs(2:1) composite catalyst exhibited nearly overlapping time-conversion curves for TCs over at least five consecutive cycles. Furthermore, after each reaction, efficient separation of the catalyst from the reaction system was achieved via simple centrifugation. The recovered catalyst was thoroughly washed with an acetonitrile/ethanol/water mixed solvent, vacuum-dried, reactivated, and then used in subsequent cycling experiments. The results showed that the conversion of TCs remained stable at around 98% after each cycle (Fig. S16), fully demonstrating the excellent catalytic stability and typical heterogeneous catalytic characteristics of PMo@VioPAFs(2:1). Based on the promoting effect of the reduced state Mo^{5+} on catalytic activity as mentioned earlier, we conducted valence state characterization of the recycled

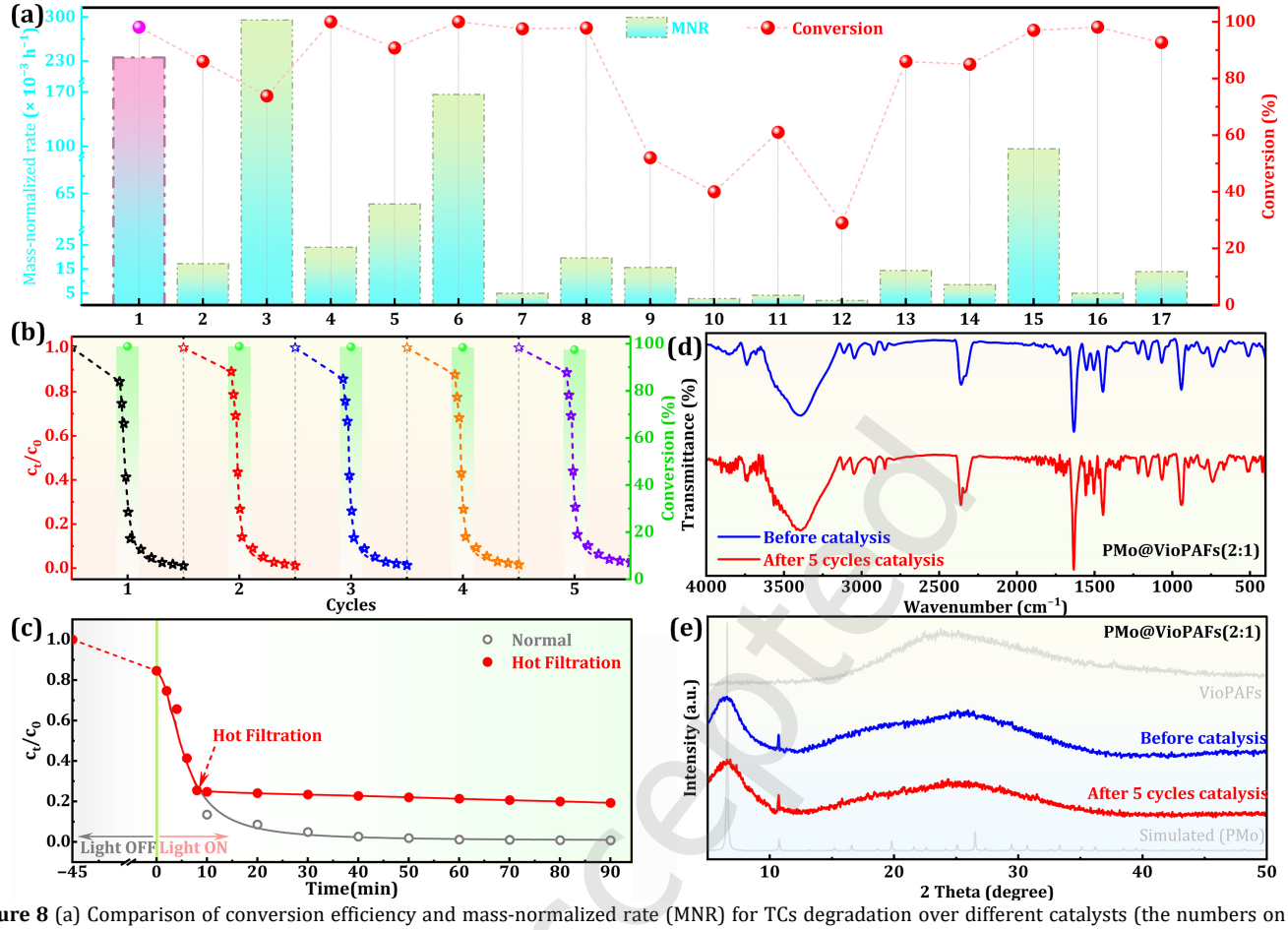

Figure 8 (a) Comparison of conversion efficiency and mass-normalized rate (MNR) for TCs degradation over different catalysts (the numbers on the horizontal axis correspond to the catalytic systems represented by each entry number in Table 1); (b) Recycling stability test of PMo@VioPAFs(2:1) in the catalytic degradation of TCs (5 cycles); (c) Hot filtration test for the degradation of TCs catalyzed by PMo@VioPAFs(2:1); (d) FT-IR spectra of the catalyst before and after the reaction; (e) PXRD patterns of the catalyst before and after the reaction.

catalysts to verify the mechanism of maintaining high activity. The results of Fig. S17 indicate that the Mo^{5+} species still remain in the recycled samples, and their relative proportion is basically the same as that of the fresh catalysts. This directly proves that the stable existence of Mo(V) species is one of the key factors for the excellent performance of the catalyst in the recycling process.

To further verify its heterogeneous catalytic nature, a hot filtration experiment was conducted (Fig. 8c). When the reaction proceeded to approximately 10 min, the solid catalyst was rapidly removed from the reaction system using a syringe filter, and the remaining filtrate was allowed to continue reacting under the same optimal conditions. It was found that after catalyst removal, the concentration of TCs in the reaction system decreased only very slightly, which may be mainly attributed to the desorption of a small amount of physically adsorbed substrate from the catalyst surface. These results clearly indicate that PMo@VioPAFs(2:1) exhibits true heterogeneous catalytic behavior in the target reaction system, with no significant leaching of active species.

Finally, the catalyst structure before and after cycling was characterized by FT-IR and PXRD (Fig. 8d-8e). The results showed that the catalyst after cycling retained the characteristic absorption peaks of polyoxometalates in the wavenumber range of 600-1100 cm^{-1}, as well as the characteristic absorption peaks of the VioPAF framework in the range of 1000-2000 cm^{-1}, almost identical to the FT-IR spectrum of the fresh catalyst. Meanwhile, the PXRD pattern after cycling was highly consistent with that before the reaction, with clear characteristic diffraction peaks of the polyoxometalate showing no significant attenuation in intensity. All the above results fully demonstrate that the synthesized PMo@VioPAFs(2:1) composite catalyst possesses typical features of a heterogeneous catalyst, maintaining excellent catalytic performance and intact crystal structure even after multiple cycles of use. Moreover, quantitative analysis of Mo element in the filtrate after the reaction revealed its concentration to be merely at trace levels, confirming an extremely low leaching rate of the PMo. This further attests to the good structural stability of the hetero-motif catalyst under the reaction conditions (Table S3).

3.8 Possible reaction mechanism

According to existing literature reports, POM@COF composite materials with hetero-motif structures mainly involve two potential mechanisms in photocatalytic reactions: energy transfer and charge transfer [58]. Through systematic optimization experiments, we found that when dissolved oxygen in the reaction system was completely removed, the degradation rate of TCs could still remain at nearly 50%. This experimental phenomenon strongly indicates the existence of an independent reaction pathway in this photocatalytic system that does not rely on molecular oxygen as an oxidant.

combining the charge separation characteristics of hetero-motif materials, we preliminarily speculate that this non-oxygen-dependent pathway may originate from the direct oxidation effect of photogenerated holes (h^+) generated during the efficient charge transfer induced by photoexcitation. Theoretically, in an oxygen-free environment, photogenerated electrons cannot yield ROS due to the lack of O_2 as an electron acceptor. Should the photogenerated h^+ be continuously consumed, the accumulation of electrons in the CB would trigger severe carrier recombination, potentially culminating in catalyst self-reduction and deactivation. However, within this specific system, the POM component affords the photogenerated electrons a definitive sink. On one hand, capitalizing on the excellent reversible redox properties of POMs, conduction band electrons are efficiently captured by the POM units and converted into reduced heteropoly blue species. This achieves reversible electron storage within the catalyst framework. This distinctive "electron buffering" effect mitigates excessive electron buildup in the CB, thereby effectively suppressing carrier recombination and ensuring the sustained oxidative degradation capability of the photogenerated holes. On the other hand, target pollutants with reducible functional groups like unsaturated double bonds can serve as weak electron acceptors. They can be directly reduced and degraded by either conduction band electrons or the electrons stored within the POM reservoirs. Consequently, anaerobic degradation is fundamentally a synergistic process involving hole-dominated oxidation coupled with direct electron reduction/storage, rather than being driven solely by holes.

To directly verify the presence of h^+ in the system and its specific contribution to TCs degradation, we conducted active species quenching experiments using ethylene diamine tetraacetic acid disodium salt (EDTA), which specifically quenches holes (Fig. 9a and S18). The experimental results showed that after adding EDTA, the degradation rate of TCs decreased from approximately 100% in the blank group to 61.3%. This data directly indicates that h^+ indeed substantially participates in the photocatalytic oxidation degradation process of TCs. This conclusion is further supported by combined quenching experiments. When TEMPO and isopropanol (IPA) were simultaneously added to the reaction system to comprehensively quench all possible reactive oxygen species ($\cdot O_2^-$ and $\cdot OH$), the degradation rate of TCs could still be maintained at around 52% (Fig. 9b). This residual degradation activity can only be attributed to the oxidation effect of unquenched photogenerated holes, further confirming the existence of h^+ as the main active species. In typical semiconductor-like photocatalytic systems, photogenerated holes are usually produced at the VB when photogenerated electrons transition from the valence band to the CB. Based on the photoelectrochemical characterization analysis, since the PMo component has a lower VB position, the charge separation generated upon photoexcitation produces h^+, and the excited electrons obtained in the CB can easily transfer to the h^+ in the VB of VioPAFs. We therefore speculate that the photogenerated holes participating in the catalytic reaction in this system mainly originate from the valence band of the PMo component.

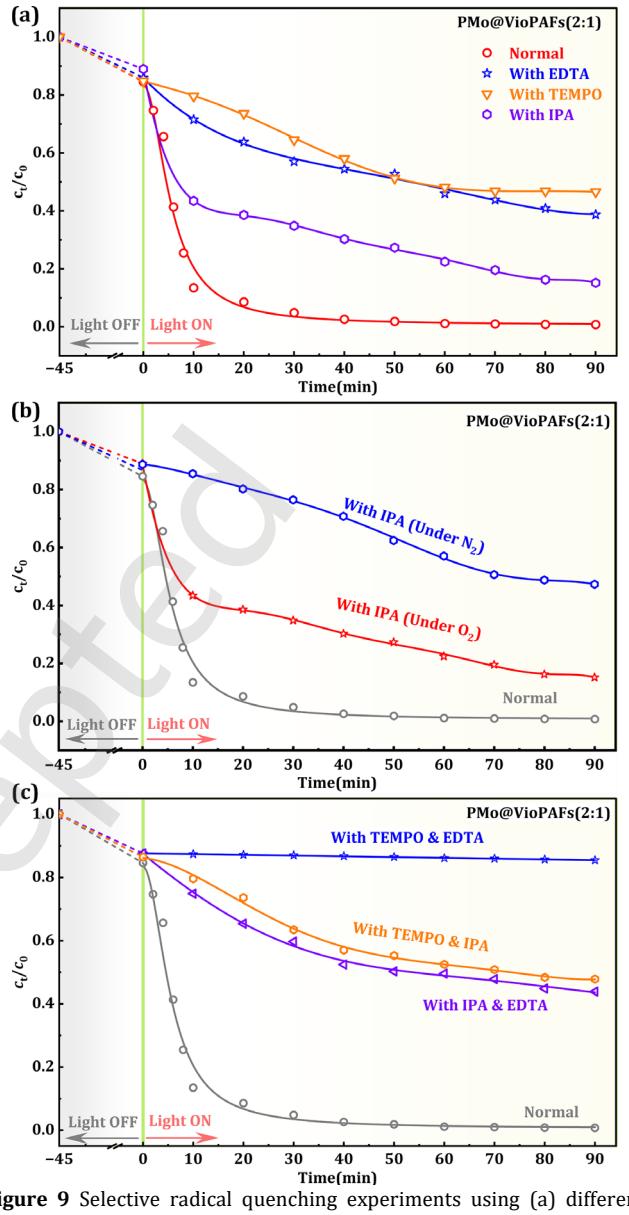

Figure 9 Selective radical quenching experiments using (a) different radical scavengers; (b) different combinations of radical scavengers; (c) in the presence of IPA radical scavenger under O_2 and N_2 atmosphere.

To further elucidate the main reactive oxygen species involved in the degradation of TCs in this photocatalytic system and their relative contributions, we conducted additional radical trapping experiments for verification. Using TEMPO as a specific quencher, a qualitative and semi-quantitative analysis of the potential superoxide radicals ($\cdot O_2^-$) in the system was performed (Fig. 9a and S18). The experimental results showed that upon adding TEMPO to the reaction system, the photocatalytic degradation efficiency of TCs significantly decreased, with the degradation rate remaining at approximately 50% after 90 min of light exposure. This result clearly indicates that $\cdot O_2^-$ is one of the crucial active species in this photocatalytic system. Combined with the earlier systematic photoelectrochemical characterization results, we speculate that the generation mechanism of $\cdot O_2^-$ can be attributed to the single-electron reduction of dissolved oxygen molecules by photogenerated electrons on the CB of VioPAFs after photoexcitation. Notably, the degradation rate obtained from the TEMPO quenching

experiment closely matches the catalytic degradation performance under a nitrogen atmosphere. This mutually corroborating experimental outcome further confirms the non-oxygen-dependent direct oxidation pathway mediated by photogenerated holes, as discussed in the previous analysis.

Furthermore, hydroxyl radicals (·OH), as one of the most common strongly oxidizing reactive oxygen species in the photocatalytic degradation of organic pollutants, also require systematic investigation regarding their presence and contribution in this system. To verify this, we introduced IPA as a specific quencher for ·OH into the reaction system. The experimental results showed that the degradation rate of TCs could still reach approximately 85% after adding IPA, indicating that ·OH does exist in the system, but its overall contribution to the degradation of TCs is relatively minor (Fig. 9a). As is well known, the generation pathways of ·OH are diverse; it can originate either from the direct oxidation of water molecules by photogenerated h^+ or from multi-step proton-coupled reduction processes involving $\cdot O_2^-$. To clarify the specific source of ·OH in this system, we designed a series of rigorous comparative experiments. First, when IPA was added to the reaction system under a N_2 atmosphere, the degradation rate of TCs was found to be approximately 52.7% (Fig. 9c), a value essentially consistent with the degradation rate under a pure N_2 atmosphere and the results of quenching experiments using TEMPO as the sole quencher. This experimental phenomenon strongly suggests that the ·OH in the system likely originates primarily from the subsequent transformation of $\cdot O_2^-$. Further supporting this inference, the EDTA quenching experiment under a nitrogen atmosphere also provided strong evidence (Fig. S19). In this experiment, the degradation rate of TCs was only 15.3%, comparable to the adsorption capacity achieved under dark conditions after reaching adsorption equilibrium. This indicates that upon removal of O_2 and complete quenching of photogenerated h^+, the photocatalytic reaction almost entirely halts, indirectly proving that the ·OH in the system does not directly originate from the oxidation of water molecules. Moreover, the results of a combined quenching experiment involving simultaneous addition of EDTA and TEMPO showed that the degradation reaction of TCs also nearly ceased completely (Fig. 9b). This cross-validated outcome further confirms that ·OH is primarily derived from the stepwise transformation of $\cdot O_2^-$, rather than the direct oxidation of water molecules by photogenerated holes.

Based on the mutually corroborating results from the aforementioned radical trapping experiments and control experiments under a nitrogen atmosphere, we preliminarily propose a possible dual-active-site synergistic dual-path photocatalytic reaction mechanism for this system. Namely, it consists of the direct oxidation pathway mediated by photogenerated holes from PMo, and the indirect oxidation pathway initiated by photogenerated electrons from VioPAFs activating molecular oxygen to generate $\cdot O_2^-$, which subsequently undergoes multi-step proton-coupled transformations to produce ·OH.

To further validate the rationality of the aforementioned dual-path reaction mechanism, we employed electron paramagnetic resonance (EPR) technology to directly monitor and quantify the reactive oxygen species generated during the photocatalytic process, using the optimal PMo@VioPAFs(2:1) composite as the model catalyst. In the experiments, *p*-benzoquinone (BQ) and 5,5-dimethyl-1-pyrroline N-oxide (DMPO) were used as specific spin-trapping agents for $\cdot O_2^-$ and ·OH, respectively. In the detection of $\cdot O_2^-$, for the PMo@VioPAFs(2:1) catalyst system, almost no radical signals were detected under dark conditions. However, upon visible light irradiation, the characteristic four-line signal of $\cdot O_2^-$ immediately appeared, and its intensity gradually increased as the irradiation time was extended from 0 to 10 min (Fig. 10a). This result directly proves the generation of $\cdot O_2^-$ during the photocatalytic reaction, with its production positively correlating with irradiation time. In the detection of ·OH, a completely consistent trend was observed: no significant signal under dark conditions, the appearance of characteristic ·OH signals upon illumination, and a gradual increase in signal intensity with prolonged irradiation time (Fig. 10b). Nonetheless, combined with the aforementioned free radical quenching results, it is clear that ·OH is not the primary reactive oxygen species in this system but rather a secondary species derived from $\cdot O_2^-$, contributing significantly less to TCs degradation than $\cdot O_2^-$.

Comparative experiments showed that the pure VioPAF framework could also generate detectable $\cdot O_2^-$ and ·OH signals under light (Fig. S20-S21). Notably, however, when VioPAFs was composited with PMo to form the hetero-motif structure, the EPR signal intensities for both $\cdot O_2^-$ and ·OH were significantly enhanced, more than doubling compared to those of pure VioPAFs (Fig. 10c-10d). This phenomenon clearly indicates that the hetero-motif structure formed between PMo and VioPAFs can effectively promote the separation and migration of photogenerated charge carriers under light excitation, thereby significantly improving the generation efficiency of reactive oxygen species and ultimately leading to superior photocatalytic degradation performance.

All the experimental results mentioned above (condition optimization, radical trapping, photoelectrochemical characterization, and direct EPR detection) corroborate each other and collectively support the proposed dual-path reaction mechanism for the photocatalytic degradation of TCs by the PMo@VioPAF hetero-motif system. The specific process of this mechanism is as follows (Scheme 2). Firstly, under visible light irradiation, both PMo and VioPAFs are excited to generate photogenerated electrons (e^-) and holes (h^+). Unlike the rapid recombination in pure PMo or pure VioPAFs, in the PMo@VioPAF hetero-motif system, due to the well-matched energy levels between the CB of PMo and the VB of VioPAFs (Fig. 4d), the photogenerated electrons on the CB of PMo can efficiently migrate to the VB of VioPAFs and recombine with the holes there. This unique charge transfer mode effectively suppresses the recombination of photogenerated electron-hole pairs in the overall system, thereby significantly prolonging the lifetime of the charge carriers. Based on this charge separation process, two parallel and independent oxidative degradation pathways are established. The first is the direct oxidation pathway. The

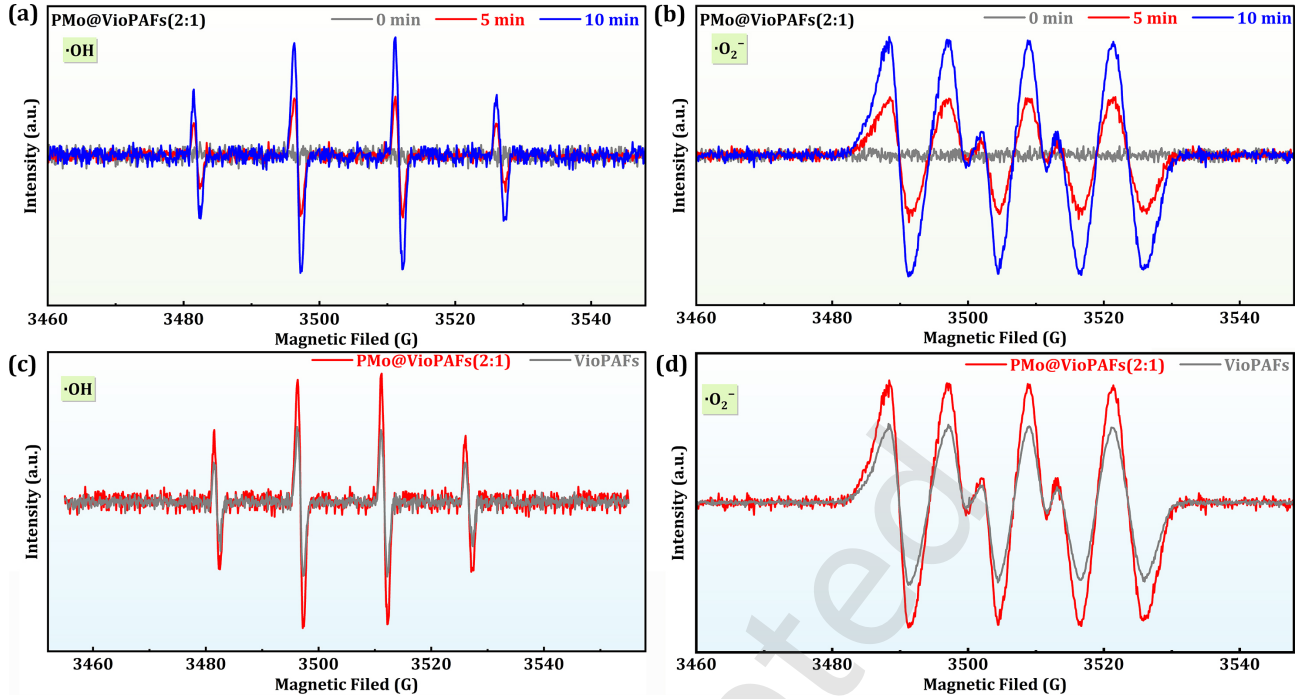

Figure 10 EPR spectrum for detecting (a) ·OH and (b) $\cdot O_2^-$ in PMo@VioPAFs(2:1) system at different times; (c) ·OH and (d) $\cdot O_2^-$ in PMo@VioPAFs(2:1) system and VioPAF system at 10 min.

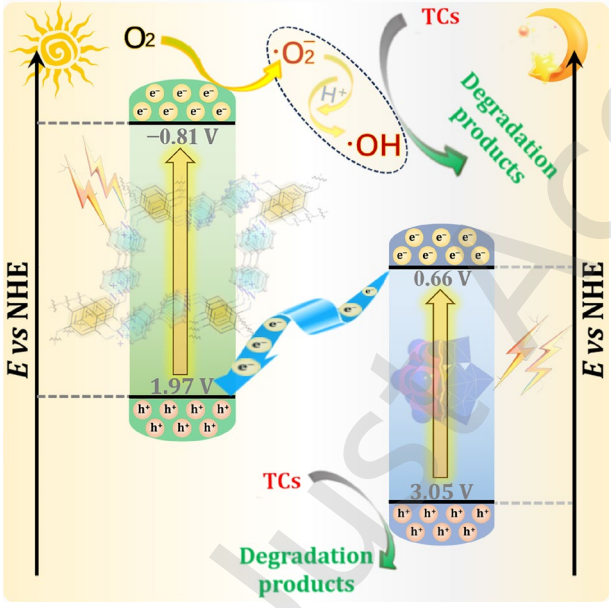

Scheme 2 The possible dual-site and dual-reaction path of PMo@VioPAFs photocatalytic TCs degradation.

highly active holes retained in the VB of PMo can directly oxidize TCs molecules adsorbed on the catalyst's active sites, gradually mineralizing them into harmless H_2O and CO_2. The second is the indirect oxidation pathway. The photogenerated electrons accumulated on the CB of VioPAFs can reduce dissolved oxygen molecules in the system to generate $\cdot O_2^-$. A portion of $\cdot O_2^-$ directly participates in the oxidative degradation of TCs. Another portion that does not react immediately undergoes multi-step protonation in the acidic reaction medium, transforming into hydrogen peroxide intermediates, which are subsequently reduced to generate ·OH, contributing to further oxidative degradation. This also explains the relatively weak contribution of ·OH to TCs degradation observed in the radical quenching experiments. As a secondary reactive species, its generation rate and reactivity are lower than those of the primary species, $\cdot O_2^-$.

Furthermore, to elucidate the photodegradation trajectory of TC and identify key intermediates, qualitative analyses were conducted on the reaction system *via* liquid chromatography-tandem mass spectrometry (LC-MS). Integrating our experimental findings with prior literature reports, we postulated two plausible degradation pathways for TC catalyzed by PMo@VioPAFs (Fig. S22 and Table S2) [5]. Pathway I is orchestrated by hydroxylation: the parent TC molecule (m/z = 445.15) undergoes sequential hydroxylative modifications, evolving into intermediates P1 (m/z = 461.15), P2 (m/z = 433.25), and P3 (m/z = 417.13). Conversely, Pathway II is characterized by N-demethylation and dehydroxylation; through the stepwise cleavage of functional groups, TC is transformed into intermediates P4 (m/z = 431.14), P5 (m/z = 417.14), and P6 (m/z=401.13). Subsequently, these intermediates from both pathways succumb to the sustained oxidative assault of reactive species, leading to aromatic ring cleavage and the formation of diverse low-molecular-weight organic compounds. Ultimately, deep mineralization ensues, converting the substrate completely into inorganic micromolecules such as CO_2, H_2O, and NH_3.

4 Conclusion

This study successfully engineered a series of novel PMo@VioPAFs featuring bi-functional hetero-motif structures for the rapid decontamination of TCs in water. By leveraging the strong electrostatic synergy between the cationic VioPAF framework and anionic PMo clusters, we achieved a composite that maintains remarkable robustness and active-site accessibility. A key finding is the viologen-induced self-reduction mechanism, which generates highly reactive low-valent Mo centers, thereby boosting catalytic

efficiency. The optimized PMo@VioPAFs(2:1) reached a near-quantitative degradation (98%) of TCs in just 50 min, demonstrating performance metrics that benchmark favorably against state-of-the-art POM-based materials. The enhanced activity is attributed to the hetero-motif structure, which accelerates charge carrier dynamics across the heterojunction. The photodegradation proceeds through a synergistic dual-track pathway, where photogenerated holes, $\cdot O_2^-$ and ·OH radicals work in concert to mineralize pollutants. Overall, this integration of POM redox chemistry with COF structural engineering offers a versatile and high-performance toolkit for the remediation of recalcitrant organic contaminants in complex aquatic matrices.

Electronic Supplementary Material: Supplementary material (including materials and instrumentation, synthesis of VioPAFs, as well as morphology, nitrogen adsorption-desorption isotherms, solid-state ^{13}C NMR, zeta potential, kinetic simulation, FTIR, PXRD, EPR, MS, Mott-Schottky diagram, and Tauc plots of the comparison catalysts, etc.) is available in the onlineversion of this article at https://doi.org/10.26599/POM.2026.9140157.

Data availability

All data needed to support the conclusions in the paper are presented in the manuscript and/or the Electronic SupplementaryMaterial. Additional data related to this paper may be requested from the corresponding author upon request.

Acknowledgements

This work was financially supported by the Hainan Provincial Natural Science Foundation of China (225QN219), the Open Fund of Key Laboratory of Electrochemical Energy Storage and Energy Conversion of Hainan Province (KFKT2024004), the Innovational Fund for Scientific and Technological Personnel of Hainan Province (KJRC2023D32), the National Natural Science Foundation of China (22361017 and 22401063), the Scientific Research Support Project of Colleges and Universities in Hainan Province (Hnky2024-12), the Research Start-up Fund of Hainan University, China (KYQD(ZR)23039), the Talent Research Initiation Fund Project of Hainan Normal University (HSZK-KYQD-202407), the Hainan Provincial Collaborative Innovation Center for Flexible Talent Introduction, and the Specific Research Fund of the Innovation Platform for Academicians of Hainan Province (YSPTZX202321).

Declaration of competing interest

All the contributing author(s) report(s) no conflict of interests in this work.

Author contribution statement

The manuscript is directed by Q.H. Pan, Y.H. Chen, X.F. Jing, and D.Y. Guo, who are also responsible for providing useful discussion and revision of the manuscript. S.Z. Chang is responsible for the guidance and design of materials, most of the performance tests, data analysis, drawing, manuscript modification and final manuscript writing. J.H. Zhang is responsible for the synthesis of materials and some property tests. Y.H. Chen is also responsible for synthesizing some materials and completing the draft of the manuscript.

Informed consent

Not applicable.

Ethics statement

Not applicable.

Use of AI statement

None.

References

[1] Brand J. A.; Michelangeli M.; Shry S. J.; Moore E. R.; Bose A. P. H.; Cerveny D.; Martin J. M.; Hellström G.; McCallum E. S., et al. Pharmaceutical Pollution Influences River-to-Sea Migration in Atlantic Salmon (Salmo Salar). *Science*, **2025**, *388*, 217–222.

[2] Souza H. d. O.; Costa R. d. S.; Quadra G. R.; Fernandez M. A. d. S. Pharmaceutical Pollution and Sustainable Development Goals: Going the Right Way? *Sustainable Chem. Pharm.*, **2021**, *21*, 100428.

[3] Rossiter S. E.; Fletcher M. H.; Wuest W. M. Natural Products as Platforms to Overcome Antibiotic Resistance. *Chem. Rev.*, **2017**, *117*, 12415–12474.

[4] Lugagne J.-B.; Dunlop M. J. Anticipating Antibiotic Resistance. *Science*, **2022**, *375*, 818–819.

[5] Lin Y.; Gan L.; Zhao X.; Che G.; Wang S.; Pan Q. Facile Synthesis of Ag/AgCl/PAF-54 Heterojunction Photocatalysts for TC Degradation. *Chem. Synth.*, **2025**, *5*, 4.

[6] Chen Y.; Huang Y.; Chen Y.; Li Y.; Sidikjan N.; Lin N.; Li Y.; Guo X.; Shen G., et al. A Systematic Review of Sources, Occurrence, Behavior and Risks of Global Marine Antibiotics. *npj Emerg. Contam.*, **2025**, *1*, 15.

[7] *Guidance on Wastewater and Solid Waste Management for Manufacturing of Antibiotics*. Geneva: World Health Organization, **2024**.

[8] Zhang Y.; Liu Y.; Gong X.; Wang Z.; Liu Y.; Wang P.; Cheng H.; Huang B.; Zheng Z. Construction of Piezoelectric Photocatalyst Au/BiVO4 for Efficient Degradation of Tetracycline and Studied at Single-Particle Level. *Chem. Synth.*, **2024**, *4*, 21.

[9] Zhu Y.-G.; Zhao Y.; Li B.; Huang C.-L.; Zhang S.-Y.; Yu S.; Chen Y.-S.; Zhang T.; Gillings M. R., et al. Continental-Scale Pollution of Estuaries with Antibiotic Resistance Genes. *Nat. Microbiol.*, **2017**, *2*, 16270.

[10] Bäumler A. J. The Coming Microbial Crisis: Our Antibiotic Bubble is about to Burst. *Science*, **2024**, *385*, eads3473.

[11] Lu J.; Zhang Y.; Wu J.; Wang J.; Cai Y. Fate of Antibiotic Resistance Genes in Reclaimed Water Reuse System with Integrated Membrane Process. *J. Hazard. Mater.*, **2020**, *382*, 121025.

[12] Jiang X.; Li C.; Chen Y.; Chen J.; Guo Z.; Zhou Q.; Zhu L.; Lin D.; Xu J. Universal Scalable Production of Single-Atom Catalysts for Antibiotic Wastewater Treatment. *Nat. Water*, **2026**, *4*, 206–216.

[13] Wang Y.; Du B.; Wu G. Tetracycline in Anaerobic Digestion: Microbial Inhibition, Removal Pathways, and Conductive Material Mitigation. *J. Hazard. Mater.*, **2025**, *496*, 139378.

[14] Yang J.; Tian S.; Song Z.; Hao Y.; Lu M. Recent advances in Sorption-Based Photocatalytic Materials for the Degradation of Antibiotics. *Coord. Chem. Rev.*, **2025**, *523*, 216257.

[15] Singh P. P.; Pandey G.; Murti Y.; Gairola J.; Mahajan S.; Kandhari H.; Tivari S.; Srivastava V. Light-Driven Photocatalysis as an Effective Tool for Degradation of Antibiotics. *RSC Adv.*, **2024**, *14*, 20492–20515.

[16] Wei Z.; Liu J.; Shangguan W. A Review on Photocatalysis in Antibiotic Wastewater: Pollutant Degradation and Hydrogen Production. *Chin. J. Catal.*, **2020**, *41*, 1440–1450.

[17] Fan B. H.; Fu Y. M.; Liu Y. Q.; Chang S. Z.; Wang F. X.; Pan Q. H. Perovskite Hydroxide $ZnSn(OH)_6$-Derived Three-Dimensional Flower-Like SnS_2/Bi_2S_3 Heterojunction for Sensitive Photoelectrochemical Detection of Cr(VI). *Rare Met.*, **2025**, *44*, 10368-10378.

[18] Fang X.; Jiang W.; Cao Y.; Lei J.; Ma X.; Chang Y.; Zhang Z.; Lv C.; Chen H., et al. Self-Adaptive Partially Oxidised W-Based Quantum Dots With Asymmetric BiS1O4 as Axial Polarisation Center for Enhanced Photocatalysis. *cMat*, **2025**, *2*, e70011.

[19] Raabe J.-C. *Polyoxometalate Chemistry*. Royal Society of Chemistry, **2026**.

[20] Shang Q.; Shen K.; Zhao D.; Wang X.; Wei Y.; Wang H.; Wang G.;

Zhang D.; Niu J. Rare-earth-induced peroxo-phosphotungstates: Enhanced proton conductivity in corresponding membranes. *Polyoxometalates*, **2025**, *4*, 9140077.

[21] Yin Y.-A.; Chen W.-J.; Liu C.-Y.; Zhang M.-M.; Lin C.-G.; Miras H. N.; Song Y.-F. Supramolecular Assembly of Covalently Modified Anderson-Type Polyoxometalates and Crown Ethers towards *pseudo*-Rotaxane Structures. *Polyoxometalates*, **2025**, *4*, 9140081.

[22] Ricciardulli T.; Gorthy S.; Adams J. S.; Thompson C.; Karim A. M.; Neurock M.; Flaherty D. W. Effect of Pd Coordination and Isolation on the Catalytic Reduction of O_2 to H_2O_2 over PdAu Bimetallic Nanoparticles. *J. Am. Chem. Soc.*, **2021**, *143*, 5445−5464.

[23] Chen H.; Gong Y.; Chu Q.; Pang X.; Huang X.; Tian X.; Yang W.; Pan Q.; Su Z., et al. Face-directed Strategy for the Construction of Polyoxovanadate-based Metal-Organic Tetrahedra. *Chem. Res. Chin. Univ.*, **2023**, *39*, 954−959.

[24] Zhao Q.; Mao D.-A.; Huang L.-L.; Zhou K.; Tian H.-R.; Chen B.-K.; Bi Y.-F. Thiacalix[4]Arene-Functionalized Molecular Clusters Involving the Keggin-Type PM_4Mo_8 (M = Co, Ni) Motif: Electrochemical and Photothermal Conversion Properties. *Polyoxometalates*, **2025**, *4*, 9140091.

[25] Lauinger S. M.; Yin Q.; Geletii Y. V.; Hill C. L., Polyoxometalate Multielectron Catalysts in Solar Fuel Production. in Advances in Inorganic Chemistry, eds. van Eldik R.; Cronin L., Academic Press, 2017, p. 117−154.

[26] Wang H.; Wu J.; Liu H.; Huang X.; Liu Y.; Yang G. One-Dimensional Mixed-Valence Ce(III)/Ce(IV)-Containing Arsenotungstate for Photocatalytic Synthesis of Quinazolines. *Chem. Commun.*, **2026**, *62*, 7830-7834.

[27] Li S.; Zheng Y.; Liu G.-C.; Li X.-H.; Zhang Z.; Wang X.-L. New Two Fold Interpenetrating 3D Polyoxovanadate-Based Metal–Organic Framework as Bifunctional Catalyst for the Removal of 2-Chloroethyl Ethyl Sulfide and Phenolic Compounds. *Polyoxometalates*, **2024**, *3*, 9140061.

[28] Ru S.; Wang T.; Zhao C.; Wang S.; He P.; Song Y.; Wei Y.; Zang D. Polyoxometalate-Based Donor–Acceptor-Type Photocatalytic-Active Cluster: Exploring Structure–Activity Relationships in Oxidation of Alkylbenzene C(sp^3)–H Bond *via* Ligand Design. *Nano Res.*, **2025**, *18*, 94908185.

[29] Jiang S.; Zhou M.; Yang G.; Li H.; Liu Y. Uranyl-Bridged Polyoxometalate Assembled from Te-Oriented Three-Layered Cage Clusters for Photocatalytic Oxy-Thiocyanation of Alkenes. *Inorg. Chem.*, **2026**, *65*, 10979-10985.

[30] Suzuki K.; Mizuno N.; Yamaguchi K. Polyoxometalate Photocatalysis for Liquid-Phase Selective Organic Functional Group Transformations. *ACS Catal.*, **2018**, *8*, 10809−10825.

[31] Song J. Y.; Chen X.; Wang Y. M.; Luo X.; Zhang T. E.; Ning G. H.; Li D. Tuning the Catalytic Activity of Covalent Metal-Organic Frameworks for CO_2 Cycloaddition Reactions. *Chem. Asian J.*, **2023**, *18*, e202300857.

[32] Li K.; Liu S.; Niu J.; Wang J. Polyoxometalate Photocatalysts for Sustainable Reactions. *Chem. Commun.*, **2026**, *62*, 1800-1819.

[33] Luo Z.; Ye X.; Zhang S.; Xue S.; Yang C.; Hou Y.; Xing W.; Yu R.; Sun J., et al. Unveiling the Charge Transfer Dynamics Steered by Built-In Electric Fields in BiOBr Photocatalysts. *Nat. Commun.*, **2022**, *13*, 2230.

[34] Zhang D.; Wang Y.; Ni H.; Sun X.; Wang Y.; Liu D.; Xu X.; Chen Y. Comparison of One-/Two-Photon Absorption Properties of D-A-D Type Zinc Phthalocyanines Constructed with Different Rylene Diimides. *Chem. Res. Chin. Univ.*, **2025**, *42*, 612-621.

[35] Zhou Y.; Liu C.; Li X.; Zhan P.; Xu X.; Peng X. Recent Advances in Piezocatalysis and Piezo-Photocatalysis in Energy and Environment: Materials, Design, and Applications. *Rare Met.*, **2026**, *45*, e70175.

[36] Wang H.; Zhang L.; Chen Z.; Hu J.; Li S.; Wang Z.; Liu J.; Wang X. Semiconductor Heterojunction Photocatalysts: Design, Construction, and Photocatalytic Performances. *Chem. Soc. Rev.*, **2014**, *43*, 5234−5244.

[37] Yoshino S.; Iwase A.; Yamaguchi Y.; Suzuki T. M.; Morikawa T.; Kudo A. Photocatalytic CO_2 Reduction Using Water as an Electron Donor under Visible Light Irradiation by Z-Scheme and Photoelectrochemical Systems over $(CuGa)_{0.5}ZnS_2$ in the Presence of Basic Additives. *J. Am. Chem. Soc.*, **2022**, *144*, 2323−2332.

[38] Yu S.; Kim Y. H.; Lee S. Y.; Song H. D.; Yi J. Hot-Electron-Transfer Enhancement for the Efficient Energy Conversion of Visible Light. *Angew. Chem., Int. Ed.*, **2014**, *53*, 11203−11207.

[39] Cheng Y.; Zhao C.-C.; Wang T.-T.; Zhang M.; Ru S.; Deng Y.; Wang W.; Wang Y.; Song Y., et al. Interfacial Engineering of Cu_9S_5@MoS_2 p-n type Heterojunction *via* In Situ Phase Separation for Highly Efficient Electrocatalytic Oxidation of 5-Hydroxymethylfurfural. *eScience*, **2026**, *6*, 100507.

[40] Tan Y.-X.; Zhang X.; Wang Y.; Yao J. Molecular Assembly of Functional Motifs for Artificial Photosynthesis. *Acc. Mater. Res.*, **2024**, *5*, 1377−1387.

[41] Chen Y.; Chang S.; Zhao J. Synergistic Catalysis in POM@MOF and POM@COF Composites: Emerging Platforms for Catalytic Oxidation of Sulfur-Containing Compounds. *Polyoxometalates*, **2026**, 10.26599/pom.2026.9140146.

[42] Ebrahimi A.; Krivosudský L.; Khodabakhshi S.; Khaleghiabbasabadi M.; Sadeghi M.; Motola M. Polyoxometalate-Based Covalent Organic Frameworks: The Next Generation of Heterogeneous Catalysts. *Coord. Chem. Rev.*, **2026**, *548*, 217201.

[43] Chang S.; Ruan B.; Zhang J.; Wu Q.; Pan Q. Recent Advances in Polyoxometalate@Porous-Framework Composite Catalysts for Oxidative Desulfurization. *Chem. Res. Chin. Univ.*, **2026**, *42*, 1045-1068.

[44] Kong S.; Zhang X.; Xu N.; Wang X. Recent Advances in Polyoxometalate-Covalent Organic Framework Composites: Rational Design, Structural Modulation, and Application Perspectives. *Dalton Trans.*, **2026**, *55*, 7429-7443.

[45] Zhu Q.; An H.; Xu T.; Chang S.; Chen Y.; Luo H.; Huang Y. PW_{12}-M@COFs as Efficient Photocatalysts for Visible-Light-Driven Oxidation of Various Sulfides and Degradation of Chemical Warfare Agent Simulant. *Appl. Catal., A*, **2023**, *662*, 119283.

[46] Geng K.; He T.; Liu R.; Dalapati S.; Tan K. T.; Li Z.; Tao S.; Gong Y.; Jiang Q., et al. Covalent Organic Frameworks: Design, Synthesis, and Functions. *Chem. Rev.*, **2020**, *120*, 8814-8933.

[47] Liu L.; Su X.; Qi M.; Gao X.; Ren H.; Chen L. Facile Synthesis of Heteroporous Covalent Organic Frameworks with Dual Linkages: a "Three-in-One" Strategy. *Chem. Synth.*, **2024**, *4*, 10.

[48] Zhang L.; Liu J.; Lan Y. Q. Hetero-Motif Molecular Junction Photocatalysts: A New Frontier in Artificial Photosynthesis. *Acc. Chem. Res.*, **2024**, *57*, 870−883.

[49] Zhu Q.; An H.; Xu T.-Q.; Chen Y.; Wei Y.; Sun H. Polyoxometalates Embedded into Covalent Triazine Frameworks Regulating Charge Transfer for Visible-Light-Driven Synthesis of Functionalized Sulfoxides and Detoxification of Mustard Gas Simulants. *ACS Sustainable Chem. Eng.*, **2024**, *12*, 1655-1665.

[50] Lu M.; Zhang M.; Liu J.; Yu T. Y.; Chang J. N.; Shang L. J.; Li S. L.; Lan Y. Q. Confining and Highly Dispersing Single Polyoxometalate Clusters in Covalent Organic Frameworks by Covalent Linkages for CO_2 Photoreduction. *J. Am. Chem. Soc.*, **2022**, *144*, 1861-1871.

[51] Chen J.; Wang J.; Liu X.; Xu N.; Li H.; Wang X. Ultrasonic-Assisted Catalytic Oxidation of Sulfide: A Highly Efficient Keggin-POM@RT-COF-1 Catalvst Activated by Sonoluminescence. *Inorg. Chem. Commun.*, **2026**, *190*, 116937.

[52] Wang P.; Jiang L.; Zou X.; Tan H.; Zhang P.; Li J.; Liu B.; Zhu G. Confining Polyoxometalate Clusters into Porous Aromatic Framework Materials for Catalytic Desulfurization of Dibenzothiophene. *ACS Appl. Mater. Interfaces*, **2020**, *12*, 25910-25919.

[53] Song J.; Li Y.; Cao P.; Jing X.; Faheem M.; Matsuo Y.; Zhu Y.; Tian Y.; Wang X., et al. Synergic Catalysts of Polyoxometalate@Cationic Porous Aromatic Frameworks: Reciprocal Modulation of Both Capture and Conversion Materials. *Adv. Mater.*, **2019**, *31*, e1902444.

[54] Liu Y.; Shi X.; Chen X.; Du Y. Viologen-COF Enables Near-Infrared Photocatalysis *via* Linker-to-Linker Charge Transfer. *Chem Catal.*, **2025**, *5*, 101395.

[55] Zhu H. J.; Xie R. K.; Chai G.; Chen Z.; Guo H.; Cao R.; Huang Y. B. Integration of Redox-Active Viologen Moiety into Bifunctional Covalent Organic Framework for Boosting Electrochemical CO_2 Overall Reaction.

Angew. Chem., Int. Ed., **2026**, *65*, e23008.

[56] Zhou Z.; Wang Z.; Blenko A. L.; Li J.; Lin W. Viologen Covalent Organic Framework Mediates Near-Infrared Light-Induced Electron Transfer for Catalytic Oxidative Coupling Reactions. *J. Am. Chem. Soc.*, **2025**, *147*, 10846−10852.

[57] Lei P.; Geng W.; Zhang H.; Zhang P.; Li J.; Du J.; Chi Y.; Hu C. Single-Cluster Polyoxometalate Catalysts *via* Modular Electrostatic Assembly on a Cationic Covalent Organic Framework for Furfural Electroreduction. *J. Mater. Chem. A*, **2026**, *14*, 8643-8653.

[58] Zhu Q.; An H.; Fu J.; Sun H.; Zhang Y.; Xu T.-Q. Dawson-Type Polyoxometalates Functionalized Porphyrin-Based Covalent Organic Frameworks for Visible-Light-Driven Oxidation of Sulfides and Detoxification of Mustard Gas Simulants. *Inorg. Chem.*, **2025**, *64*, 16223−16233.

[59] Chang S. Z.; Zhong H. X.; Chen Y. H.; Lin Y. H.; Wang F. X.; Fu Y. M.; Pan Q. H. Multi-Stimuli-Responsive Chromic Switching Self-Assembled with Polyoxometalate and Copper-Viologen Frameworks. *cMat*, **2024**, *1*, e22.

[60] Zhu Q.; An H.; Wei Y.; Sun H.; Fu J.; Xu T.-Q. Confining Polyoxometalates in Porphyrin-Based Porous Cationic Polymer toward Boosting Visible-Light-Driven Synthesis of Sulfoxides and Detoxification of Mustard Gas Simulants. *J. Catal.*, **2024**, *436*, 115627.

[61] Yang Y.; Cong M.; Jing X.; Liu J. Synthesis of Low-cost Quaternary Ammonium Porous Materials and Their Ammonia Adsorption Performance. *Chem. J. Chin. Univ.*, **2024**, *45*, 20230438.

[62] Lin Y.; Zhao X.; Chang S.; Zhang Y.; Gan L.; Tian Y.; Pan Q.; Zhu G. Enhancing Oxidative Desulfurization of Polyoxometalate by Integrating with a Self-Reductive Framework. *Sci. China Mater.*, **2024**, *67*, 2925−2933.

[63] Zheng H.; Wang C.; Zhang X.; Li Y.; Ma H.; Liu Y. Control over Energy Level Match in Keggin Polyoxometallate-TiO_2 Microspheres for Multielectron Photocatalytic Reactions. *Appl. Catal., B*, **2018**, *234*, 79−89.

[64] Ollis D. F. Kinetics of Photocatalyzed Reactions: Five Lessons Learned. *Front. Chem.*, **2018**, *6*, 378.

[65] Shi H.; Zhu H.; Jin T.; Chen L.; Zhang J.; Qiao K.; Chen Z. Construction of Bi/Polyoxometalate Doped TiO_2 composite with Efficient Visible-Light Photocatalytic Performance: Mechanism Insight, Degradation Pathway and Toxicity Evaluation. *Appl. Surf. Sci.*, **2023**, *615*, 156310.

[66] Jiang B.; Wang T.; Li F.; Li D.; Yang Y.; Yu H.; Dong X. Polyoxometalate as Pivotal Interface in SnO_2@PW_{12}@TiO_2 Coaxial Nanofibers: From Heterojunction Design to Photocatalytic and Gas Sensing Applications. *Sens. Actuators, B*, **2023**, *390*, 133928.

[67] Sun P.; Zhou S.; Yang Y.; Liu S.; Cao Q.; Wang Y.; Wågberg T.; Hu G. Artificial Chloroplast-Like Phosphotungstic Acid-Iron Oxide Microbox Heterojunctions Penetrated by Carbon Nanotubes for solar photocatalytic degradation of Tetracycline Antibiotics in Wastewater. *Adv. Compos. Hybrid Mater.*, **2022**, *5*, 3158−3175.

[68] Xing C.; Ma M.; Chang J.; Ji Z.; Wang P.; Sun L.; Li S.; Li M. Polyoxometalate Anchored Zinc Oxide Nanocomposite as a Highly Effective Photocatalyst and Bactericide for Wastewater Decontamination. *Chem. Eng. J.*, **2023**, *464*, 142632.

[69] Yang G.; Liang Y.; Zheng H.; Zhang X.; Jia J. Fe-Polyoxometalate Nanodots Decorated Bi_2MoO_6 Nanosheets with Dominant {0 1 0} Facets for Photo-Fenton Degradation of Antibiotics over a Wide pH Range: Mechanism Insight and Toxicity Assessment. *Sep. Purif. Technol.*, **2023**, *310*, 123167.

[70] Cui Y.; Xing Z.; Guo M.; Qiu Y.; Fang B.; Li Z.; Yang S.; Zhou W. Hollow Core-Shell Potassium Phosphomolybdate@Cadmium Sulfide@Bismuth sulfide Z-Scheme Tandem Heterojunctions toward Optimized Photothermal-Photocatalytic Performance. *J. Colloid Interface Sci.*, **2022**, *607*, 942−953.

[71] Zhu H.; Shi H.; Li J.; Qu X.; Zhao S.; Wang H.; Rong A.; Chen Z. Construction of S-Scheme $Cs_3PMo_{12}O_{40}$/$MnIn_2S_4$ Heterojunction for Efficient Photocatalytic Removal of Antibiotics: Degradation Pathways, Toxicity Evaluation and Mechanism Insight. *J. Alloys Compd.*, **2024**, *976*, 173072.

[72] Zhao X.; Zhang Y.; Zhao Y.; Tan H.; Zhao Z.; Shi H.; Wang E.; Li Y. $Ag_xH_{3-x}PMo_{12}O_{40}$/Ag Nanorods/g-$C_3N_4$ 1D/2D Z-Scheme Heterojunction for Highly Efficient Visible-Light Photocatalysis. *Dalton Trans.*, **2019**, *48*, 6484−6491.

[73] Wang X.; Song Y.; Li F.; Xu W.; Zheng Y.; Xu L. A "Concentration-Induced Self-Assembly" Strategy for $Ag_xH_{3-x}PMo_{12}O_{40}$ Nanorods: Synthesis, Photoelectric Properties and Photocatalytic Applications. *Nanoscale Adv.*, **2021**, *3*, 446−454.

[74] Akbari Beni F.; Gholami A.; Ayati A.; Niknam Shahrak M.; Sillanpää M. UV-Switchable Phosphotungstic Acid Sandwiched between ZIF-8 and Au Nanoparticles to Improve Simultaneous Adsorption and UV Light Photocatalysis toward Tetracycline Degradation. *Microporous Mesoporous Mater.*, **2020**, *303*, 110275.

[75] Chen S.; Li F.; Li T.; Cao W. Loading AgCl@Ag on Phosphotungstic Acid Modified Macrocyclic Coordination Compound: Z-Scheme Photocatalyst for Persistent Pollutant Degradation and Hydrogen Evolution. *J. Colloid Interface Sci.*, **2019**, *547*, 50−59.

[76] Fu Y.; Xu Y.; Mao Y.; Tan M.; He Q.; Mao H.; Du H.; Hao D.; Wang Q. Multi-Functional Ag/Ag_3PO_4/AgPMo with S-Scheme Heterojunction for Boosted Photocatalytic Performance. *Sep. Purif. Technol.*, **2023**, *317*, 123922.

[77] Ren C.; Zhang X.; Chen C.; Niu Y. Synthesis of Polyoxometalate Compounds based on 4-Pyridine Carboxylic Acid Ligands and Their Photocatalytic Degradation of Tetracycline. *J. Mol. Struct.*, **2024**, *1316*, 139062.

Table of Contents

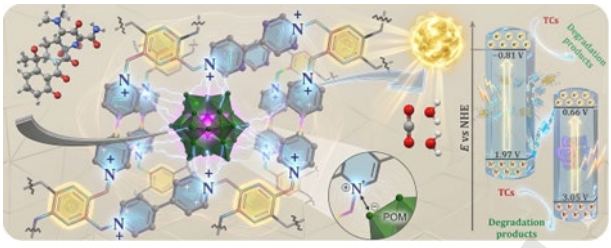

A novel polyoxomolybdate-based viologen porous aromatic frameworks (PMo@VioPAF) composite with hetero-motif structures is synthesized via mild self-assembly, enabling superior visible-light-driven photocatalytic degradation of antibiotics. The optimized material achieves >98% tetracycline removal in 50 min through a synergistic dual-site, dual-track degradation pathway, providing a powerful design strategy for efficient wastewater remediation.